

Computational Study of Non-Reactive Swirling Flow Using Hybrid Finite-Volume/Particle Method

by

Ismail Filiz

**A Thesis Submitted to the
Graduate School of Engineering
in Partial Fulfillment of the Requirements for
the Degree of**

Master of Science

in

Mechanical Engineering

Koc University

September 2009

Koc University
Graduate School of Sciences and Engineering

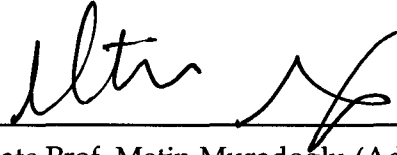
Koc University
Graduate School of Sciences and Engineering

This is to certify that I have examined this copy of a master's thesis by

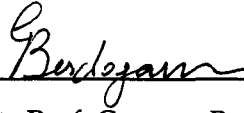
Ismail Filiz

and have found that it is complete and satisfactory in all respects,
and that any and all revisions required by the final
examining committee has been made.

Committee Members



Associate Prof. Metin Muradoglu (Advisor)



Associate Prof. Cagatay Basdogan



Assistant Prof. Mehmet Sayar

Date: 07/10/2009

ABSTRACT

This thesis computationally examines the flow characteristics of a non-reacting swirling bluff-body turbulent flow by the velocity-turbulent frequency PDF method to show the performance of the PDF method for such flows. This is the first step in performing full PDF computations of the swirling combustors and lays foundation for future work in which reacting case will be studied. In PDF method, the transport equation for mass-weighted joint PDF is directly derived from the Navier-Stokes equations and the unclosed terms are modeled through construction of stochastic differential equations (SDEs). The closure is usually guided by existent Reynolds stress models such that the joint PDF model is equivalent to the corresponding Reynolds stress model at the second moment level. The modeled PDF evolution equation is solved using a finite-volume/particle-based Monte Carlo method. The statistical stationarity of simulations is demonstrated and the computational results are compared with the experimental data. It is found that there is a reasonably good agreement between the computational and experimental results especially for the axial mean velocity and Reynolds stresses. However the prediction of the tangential mean velocity component is found to be poor indicating that the current hybrid algorithm needs further improvements.

OZET

Bu çalışmada, bir küt cismin gerisindeki reaksiyon içermeyen dögülu ve türbölanslı akımın olasılık yoğunluk fonksiyonu (OYF) yöntemiyle simölasyonu yapılmış ve OYF yönteminin bu tür karmaşık akışlar için performansı araştırılmıştır. Bu çalışma dögülu yanma odalarının OYF yöntemi ile simölasyonunun yapılması amacıyla araştırma programının ilk adımıdır ve ilerde yapılacak çalışmalara temel teşkil etmektedir. OYF yönteminde, bileşik OYF evölüsyon denklemi doğrudan Navier-Stokes denklemlerinden elde edilmekte ve açık kalan terimler stokastik diferansiyel denklemler vasıtası ile modellenmektedir. Bu işlemden mevcut Reynolds stres modelleri yol gösterici olmakta ve modellenmiş OYF yönteminin ikincil moment seviyesinde Reynolds stres modelleriyle eşdeğer olması hedeflenmektedir. Modellenmiş OYF evölüsyon denklemi tutarlı sonlu-hacimler/partikül-tabanlı Monte Carlo yöntemiyle çözülmüştür. İlk olarak simölasyonların istatistiksel olarak kararlı duruma ulaştığı gösterilmiş ve simölasyon sonuçları deneysel sonuçlarla karşılaştırılmıştır. Sayısal sonuçların özellikle aksenal ve radyal yöndeki ortalama hız bileşenleri ve Reynolds stresler için deneysel sonuçlarla uyumlu olduğu gözlenmiş ama dögü yönündeki sayısal sonuçların yeteri kadar iyi olmadığı sonucuna ulaşılmıştır.

ACKNOWLEDGEMENT

First and foremost, I offer my sincerest gratitude to my supervisor, Asst. Prof. Dr. Metin Muradoglu, who has supported me throughout my thesis with his patience and knowledge. This thesis would not have been completed or written without him. One simply could not wish for a better or friendlier supervisor. I am also grateful to Asst. Prof. Dr. Cagatay Basdogan and Asst. Prof. Dr. Mehmet Sayar, for their participation in my thesis committee.

I would like to thank all my friends at Koc University who made two years an enjoyable period of time especially Tolga Bayrak, Onder Varol, Ahmet Canberk Manav, Ilkin Kokal, Cinar Ersanli, Kamil Kiraz, Erdem Yuksel, Osman Sahin and Cansu Gulbas.

Last, I would like to thank my parents Ayse Filiz, Hasan Filiz and my sisters Ozlem Filiz and Ozer Filiz, for their love and support throughout my life, without their love and encouragement I would not be what I am today. I am very fortunate to be a part of such a great family.

TABLE OF CONTENT

| | |
|--|-------------|
| ABSTRACT | iii |
| OZET | iv |
| ACKNOWLEDGEMENT | v |
| TABLE OF CONTENT | vi |
| LIST OF TABLES | vii |
| LIST OF FIGURES | viii |
| NOMENCLATURE | x |
| INTRODUCTION | 1 |
| JOINT PDF MODELING OF TURBULENT FLOW | 7 |
| 2.1. Introduction | 7 |
| 2.2 Joint PDF Formulation | 8 |
| 2.2.1 Velocity Model | 9 |
| 2.2.2 Turbulent Frequency Model | 11 |
| 2.2.3 Chemistry and Mixing Models | 12 |
| 2.2.4 Modeled Joint PDF Evolution Equation | 13 |
| 2.3 Equations Solved by the Hybrid Method | 14 |
| 2.3.1 Mean Flow Equations Solved by the FV Method | 15 |
| 2.3.2 Equations Solved by the Particle Algorithm | 15 |
| NUMERICAL METHOD | 17 |
| 3.1 Finite Volume Scheme | 17 |
| 3.1.1 Axi-Symmetric Equations | 18 |
| 3.1.2 Finite Volume Method | 19 |
| 3.1.3 SIMPLE Method | 23 |
| 3.2. Particle Method | 26 |
| 3.3 Coupled FV/Particle Algorithm | 27 |
| RESULTS AND DISCUSSIONS | 29 |
| 4.1 Introduction | 29 |
| 4.2 Experimental Setup | 29 |
| 4.3 Computational Domain and Computational Grid | 33 |
| 4.4. Boundary Conditions | 35 |
| 4.5. Simulations | 36 |
| CONCLUSIONS AND COMMENTS | 53 |
| BIBLIOGRAPHY | 55 |
| Vita | 59 |

LIST OF TABLES

| | |
|---|----|
| Table 2.1: Model constants..... | 12 |
| Table 2.2: The model constants for the SLM model..... | 12 |
| Table 4.1: Investigated flow conditions..... | 32 |
| Table 4.2: Number of cells used in three regions in different grids. Region 1, 2 and 3 denote jet, bluff-body and co-flow regions, respectively..... | 35 |
| Table 4.3: Six selected locations in the bluff-body computational domain to monitor grid convergence. $D_b = 50$ mm is bluff-body diameter and $R_j = 1.8$ mm is jet radius..... | 37 |

LIST OF FIGURES

| | |
|---|----|
| Figure 3.1: A collocated FV grid. Mean fields are stored in the center of the cells. E, W, S, N denotes the centers of the Eastern, Western, Southern, and Northern cells, respectively. Cell faces are denoted by e, w, s, n for Eastern, Western, Southern and Northern cell faces, respectively. Length of the eastern cell face is denoted as S_e | 20 |
| Figure 4.1: Sketch of the swirling bluff-body flows. The diameter of the bluff-body is denoted by D_b . Axial and radial lengths of the computational domain are set to $15D_b$ and $3D_b$, respectively. The boundaries of the computational domain are shown in red. | 31 |
| Figure 4.2: 3D technical drawings of the Sydney Swirl Burner from different angles. | 33 |
| Figure 4.3: A coarse computational grid with number of grid parts in the axial and radial directions, $n_z=25$ and $n_r=20$, respectively. | 34 |
| Figure 4.4: Convergence histories of (a) the mean turbulent kinetic energy and (b) the mean axial velocity for non-reacting swirling bluff-body flow. | 40 |
| Figure 4.5: Mean axial velocity contour plots. (a) Computational (b) Experimental. | 41 |
| Figure 4.6: Mean tangential velocity contour plots. (a) Computational (b) Experimental. | 42 |
| Figure 4.7: (a) Experimental and (b) computational statistically steady state velocity vector field in the recirculation zone behind the bluff-body. | 43 |
| | 44 |
| Figure 4.8: Computed statistically steady state streamlines for the non-reacting swirling bluff-body flow. | 44 |
| Figure 4.9a: Mean axial velocity profiles at the axial distances of $z/D_b = 0.136$, $z/D_b = 0.2$, $z/D_b = 0.5$ and $z/D_b = 0.6$ from left to right and top to bottom, respectively. | 45 |
| Figure 4.9b: Mean axial velocity profiles at the axial distances of $z/D_b = 0.8$, $z/D_b = 1.2$, $z/D_b = 2$ and $z/D_b = 2.5$ from left to right and top to bottom, respectively. | 46 |
| Figure 4.10a: Statistically steady mean tangential velocity profiles at the axial distances of $z/D_b = 0.136$, $z/D_b = 0.2$, $z/D_b = 0.5$ and $z/D_b = 0.6$ from left to right and top to bottom, respectively. | 47 |
| Figure 4.10b: Statistically steady mean tangential velocity profiles at the axial distances of $z/D_b = 0.8$, $z/D_b = 1.2$, $z/D_b = 2$ and $z/D_b = 2.5$ from left to right and top to bottom, respectively. | 48 |
| Figure 4.11a: Statistically steady mean axial velocity profiles computed using the grid resolutions of 64×64 , 96×96 , 128×128 and 160×160 at the axial distances of $z/D_b = 0.136$, $z/D_b = 0.2$, $z/D_b = 0.5$ and $z/D_b = 0.6$ from left to right and top to bottom, respectively. | 49 |

Figure 4.11b: Statistically steady mean axial velocity profiles computed using the grid resolutions of 64x64, 96x96, 128x128 and 160x160 at the axial distances of $z/D_b = 0.8$, $z/D_b = 1.2$, $z/D_b = 2.0$ and $z/D_b = 2.5$ from left to right and top to bottom, respectively...50

Figure 4.12a: Statistically steady mean tangential velocity profiles computed using the grid resolutions of 64x64, 96x96, 128x128 and 160x160 at the axial distances of $z/D_b = 0.136$, $z/D_b = 0.2$, $z/D_b = 0.5$ and $z/D_b = 0.6$ from left to right and top to bottom, respectively.....51

Figure 4.12b: Statistically steady mean tangential velocity profiles computed using the grid resolutions of 64x64, 96x96, 128x128 and 160x160 at the axial distances of $z/D_b = 0.8$, $z/D_b = 1.2$, $z/D_b = 2.0$ and $z/D_b = 2.5$ from left to right and top to bottom, respectively.....52

NOMENCLATURE

| | |
|-------------|---------------------------------|
| RANS | Reynolds Averaged Navier Stokes |
| FV | Finite Volume |
| g_z | gravitational acceleration |
| p | pressure |
| PDF | Probability Density Function |
| r and z | radial and axial coordinates |
| R_j | radius of the jet region |
| Re | Reynolds number |
| D_b | diameter of the bluff-body |
| R_b | radius of the bluff-body |
| ρ | density |
| t | physical time |
| U | velocity scale |
| S_g | swirl number |

Chapter 1

INTRODUCTION

Both non-reacting and reacting swirling turbulent flows are ubiquitous in a wide range of engineering applications and industries such as internal combustion engines, gas turbines, burners, chemical processing plants, rotary kilns and spray dryers [2]. Due to their enhanced mixing characteristics, improved flame stability and ease of combustion control characteristics and promising performance on ignition and flame stabilization, swirl combustors have been widely used in various industrial combustors [5]. One of the leading automotive companies, Ford Motor Company, has been using newly developed swirling fuel injectors that is capable of taking advantage of swirl motion of air/fuel mixture throughout the entire combustion chamber, thereby creating a more efficient charge burn [20]. Thus, the interaction between swirl flow and combustion has been an attractive theme of investigation among a number of combustion researchers [1, 33, 19] for a long time. However, the fluid dynamics underlying swirl combustion is not fully understood limiting the choice of means available to control flame behavior in swirl combustion. The reason is that such flows often exhibit hydrodynamic instabilities, vortex breakdowns and re-circulating zones, which are difficult to resolve both experimentally and computationally. In spite of these difficulties, the enhanced mixing and stabilization of the flame caused by the swirl are desirable features [33].

Several experimental attempts have been conducted to investigate the effects of swirl on the flow and flame dynamics in combustion systems. Tangirala et al. [35] studied the influence of swirl and heat release on the flow structures and flame properties

in a non-premixed swirl burner. Their results showed that mixing and flame stability can be improved by increasing the swirl number up to approximate unity beyond which further increase in swirl actually reduces the turbulence level and flame stability. Broda et al. [3] and Seo [30] performed an experimental study of combustion dynamics in a lean-premixed swirl stabilized combustor. According to their findings, an increase in swirl number tends to decrease the instability amplitude. Presser et al. [32] studied the effects of swirl on droplet transport process in swirling spray flames. They revealed the complex spray flame structure and showed that swirl greatly modifies the flow field, droplet distribution and number density. They found that the larger droplets travel downstream relatively unperturbed but the smaller droplets are entrained by the circulating aerodynamic pattern. In addition, instabilities result in clustering of droplets in further downstream. Masri et al. [19] examined the compositional structure of the swirl-stabilized turbulent non-premixed flames using Raman-Rayleigh-LIF technique. They found that increasing the swirl number enhances the stability of the flames but increases the unburnt fuel samples even when it is far from the global blow-off limit. They also confirmed that swirl enhances the mixing. Stein and Kempf [31] performed LES computations of the Sydney swirl flames and examined the flow and mixing characteristics of this class of flames. Kempf et al.[15] also performed LES simulations of the same flames and successfully resolved the recirculation zone and vortex breakdown. They found that the computational results are in good agreement with the experimental data for the non-reacting cases but results were less satisfactory for the reacting cases. Kulsheimer and Buchner [16] investigated the combustion dynamics of swirling flames experimentally.

However, in the most of these studies, the flow is confined rendering the problem of the computing such flows extremely difficult. Confinement and sudden expansion are known to exacerbate jet processing and acoustic instabilities. The upstream flow field

close to a swirling inlet, including the vortex breakdown region can also become significantly influenced by downstream conditions at the exit plane for a confined swirling flow [31, 18, 19]. This then requires that more stringent specification of (down stream) boundary conditions be necessary. A simplification is, therefore, needed to make the problem tractable and to allow for real progress to be made in the numerical simulation of such flows. To this end, Masri et al. [1] investigated the flow structure of simple, well defined, both reacting and non-reactive swirling jets using Sydney Swirl Burner. In this work, they have focused on unconfined swirling flows of air surrounding a bluff body having a central jet of fuel. Only one co-flowing primary annular air stream is swirled. In this study, velocity field measurements have been presented for a range of conditions and swirl numbers providing a comprehensive understanding of swirling jets and flames. Since Sydney swirl burner has provided an improved understanding of swirl flows and relatively simple flow structure and well defined boundary conditions, a non-reacting swirling test case labeled as N16S159 is selected here as test case. The goal is to test the performance of the PDF method for capturing the flow field of such a complex turbulent flow. This is the first step in developing a PDF method for simulation of complex swirl burners and lays foundations for future study.

The Sydney swirl flame series have been investigated computationally mainly using Large Eddy Simulation (LES) [31, 15, 32, and 17]. Stein and Kempf [31] have studied some specific reacting and non-reacting cases using LES method to predict the velocity fields and observe the phenomena like vortex breakdown observed experimentally by Masri et al. [5]. Stein et al. [32] have also performed LES computations of the same flame series and primarily discussed the numerical issues related to the LES approach. Malalasekara et al. [17] have simulated the non-reacting swirling bluff-body flows using again an LES technique. They confirmed that the combination of lower swirl number and higher axial velocity of the primary annulus

results in the vortex breakdown as observed experimentally by Masri et al. [1]. However, the performance of the PDF approach has been not investigated for this class of burners.

Unlike other computational studies on swirling flow in literature explained briefly above, this thesis examines the flow field of a selected non-premixed case of Sydney Swirl burner series by Probability Density Function (PDF) method. In comparison to the traditional turbulence models, PDF method has been shown to be a powerful tool for modeling of complex reactive turbulent flows owing to its distinct advantages of being able to treat the important processes of convection and non-linear chemical reactions without any assumptions or approximations. These unique features allow the joint PDF method coupled with a detailed chemistry mechanism to be able to model the challenging processes of local extinction and re-ignition, i.e., the key processes that critically influence the stability of turbulent flames, quality of combustion and air pollution [34, 37]. In PDF methods, the closure is achieved through a modeled transport equation for a one-point, one-time PDF of selected flow properties. The effects of the mean pressure gradient and the body forces are presented in closed form and only fluctuating pressure gradient and molecular transport terms need to be modeled. The unclosed terms are closed through construction of stochastic differential equations that represent the same PDF as the turbulent flows [25, 28, 12]. In order to model the evolution of fluid particles in velocity-sample-space, various Langevin models have been developed. These velocity models are usually constructed such that the resulting PDF model is equivalent to an existing Reynolds stress model at the level of second moment closure. Although there are more advanced and potentially much better velocity models, the simplest possible Langevin model, i.e., the Simplified Langevin model (SLM) has been widely used mainly due to the lack of a reliable and efficient numerical solution algorithm that can be used to evaluate and improve performance of the velocity models in predicting properties of complex reacting turbulent flows of practical importance. The SLM is equivalent to the

Rotta's model at the second moment closure level and is also employed here as velocity model. In order to solve the numerical difficulties mentioned above and make the PDF methodology a feasible design tool in practical applications, the consistent hybrid finite-volume (FV)/particle-based Monte Carlo method [13, 9, 22] have been recently developed. It has been demonstrated that the hybrid method is computationally more efficient than the best alternative approaches by as much as a factor of 50 or more in terms of CPU time. The main advantage of the hybrid method comes from the fact that it combines best features of the FV and particle methods and avoids their deficiencies when they are used alone. It has been shown that it virtually eliminates the bias error and significantly reduces the statistical noise in mean fields [2, 29, 10]. In addition, the hybrid method can be easily coupled with existing flow solvers including the commercial CFD packages. In the hybrid method, a finite-volume solver is used to solve the mean mass, momentum and energy conservation equations while a particle-based Monte-Carlo algorithm is employed to solve the transport equation of the joint PDF of the fluctuating velocity, turbulent frequency and compositions. The method is completely consistent at the level of governing equations and the full consistency at the numerical solution level is achieved through correction algorithms. A local time stepping algorithm has been used in order to further improve the performance of the hybrid method [23]. The hybrid algorithm has been recently improved in terms of robustness by replacing the density based finite volume solver used Muradoglu et al.[13, 22] with a pressure-based SIMPLE type FV solver [24].

In the present study, the new hybrid algorithm has been used to study non-reacting swirling bluff-body flow in order to show the performance of the PDF approach to simulate the flow field of such as complicated and computationally challenging test case. As mentioned before, the main goal here is to lay the foundation for a future study in which the reacting versions of this flow will be studied using the PDF approach. Flow

is assumed to be statistically axisymmetric with non-zero tangential velocity component. In addition to the axisymmetric momentum equations in radial and axial directions, the tangential momentum equation has been also solved for this purpose. Flow is assumed to be incompressible and isothermal so that density remains constant. The method is applied to the swirling non-reacting bluff-body flow studied experimentally by Masri et al [1] and the results are compared with the experimental data. The flow is statistically stationary so that it is first demonstrated that the computational results reach a statistically stationary state. Then the grid convergence is examined and finally the computational results are compared with the experimental data.

The thesis is organized into four main parts. In the next chapter, the PDF method is briefly reviewed and the model equations are described. The numerical solution algorithm is discussed in Chapter 3. In this chapter, the hybrid algorithm is briefly reviewed and the present version is described in details. In Chapter 4, the Sydney swirl burner experiment conducted by Masri is first explained in details. Then some details on computational domain used in this thesis and grid generation are described. Finally, the results obtained by the current hybrid algorithm are presented and compared with the experimental data. At the end of the chapter, limitations and some numerical difficulties of the hybrid algorithm are discussed in details in terms of the stability and accuracy of the algorithm and future work is explained briefly. Some conclusions are presented in Chapter 5.

Chapter 2

JOINT PDF MODELING OF TURBULENT FLOW

2.1. Introduction

The joint PDF method is briefly reviewed and the model equations are described in this chapter. Although the flow studied in this thesis is non-reacting, the method is described for the reacting flows since the ultimate goal is to simulate the reacting turbulent flows and the PDF method really has advantages for the reacting cases. The joint probability density function (PDF) method has proven to be a successful approach for modeling reacting turbulent flows [25]. In PDF methods, turbulence closure is achieved through a modeled transport equation for the one-point, one-time PDF of selected flow properties. In this approach the convection and non-linear chemical reaction are represented exactly without modeling assumptions—a capability not possible by any other approaches. In addition, body forces and the mean pressure gradient also appear in closed form but the fluctuating pressure gradient and molecular transport terms need to be modeled. In particular, the exact treatment of the non-linear chemical reactions makes the PDF method very attractive for computations of turbulent reacting flows. It has been shown that the PDF approach is very successful to correctly resolve the important processes of local extinction and re-ignition [34, 37], which are primarily responsible for poor combustion efficiency and air pollution.

2.2 Joint PDF Formulation

The one-point, one-time mass-weighted joint PDF of velocity and compositions

$\phi = (\phi_1, \phi_2, \dots, \phi_{n_\phi})$ at location \mathbf{x} and time t is defined as

$$\langle \rho \rangle \tilde{f}'(\mathbf{V}, \boldsymbol{\psi}; \mathbf{x}, t) \equiv \rho(\boldsymbol{\psi}) \langle \delta(\mathbf{V} - \mathbf{U}) \delta(\boldsymbol{\psi} - \boldsymbol{\phi}) \rangle, \quad (2.1)$$

where ρ is the density, $\mathbf{V} = (V_1, V_2, V_3)$ and $\boldsymbol{\psi} = (\psi_1, \psi_2, \dots, \psi_{n_\psi})$ are the sample space variables for velocity \mathbf{U} and the compositions $\boldsymbol{\phi}$, respectively. The transport equation for $\tilde{f}'^\circ(\mathbf{V}, \boldsymbol{\psi}; \mathbf{x}, t)$ can be derived from the Navier-Stokes equations and species mass conservation equations using the standard techniques [25] and is given by

$$\begin{aligned} \frac{\partial \langle \rho \rangle \tilde{f}'}{\partial t} + V_j \frac{\partial \langle \rho \rangle \tilde{f}'}{\partial x_j} - \frac{\partial \langle \rho \rangle}{\partial x_j} \frac{\partial \tilde{f}'}{\partial V_j} + \frac{\partial}{\partial \psi_\alpha} (\langle \rho \rangle S_\alpha \tilde{f}') \\ = \frac{\partial}{\partial V_j} \left(\left\langle -\frac{\partial \tau_{ij}}{\partial x_i} + \frac{\partial p'}{\partial x_j} \middle| \mathbf{V}, \boldsymbol{\psi} \right\rangle \tilde{f}' \right) + \frac{\partial}{\partial \psi_\alpha} \left(\left\langle \frac{\partial J_i^\alpha}{\partial x_i} \middle| \mathbf{V}, \boldsymbol{\psi} \right\rangle \tilde{f}' \right), \end{aligned} \quad (2.2)$$

where brackets with vertical bar $\langle \dots | \dots \rangle$ stands for the conditional expectation. Summation is implied by repeating indices. As can be seen in Eq. (2.2), \tilde{f}' evolves in $(7 + n_s)$ dimensional space for a three-dimensional unsteady flow, where n_s is the number of species. All terms on the left-hand side of Eq. (2.2) are in closed form and are treated exactly but the terms on the right hand side are not closed and need to be modeled. The unclosed terms represent the transport in the velocity space due to fluctuating pressure gradient $\frac{\partial p'}{\partial x_j}$, the transport by the molecular viscous stresses τ_{ij} and transport in the composition space by the molecular diffusion J_i^α (of the scalar α in direction i). The

unclosed terms are modeled through construction of stochastic differential equations as discussed below.

2.2.1 Velocity Model

Viscous dissipation and fluctuating pressure gradient are modeled through a velocity model and the Langevin models have been widely used in the PDF methods for this purpose [25, 27]. The most general form of the Langevin model can be written as [8]

$$dU_i(t) = -\frac{1}{\langle \rho \rangle} \frac{\partial \langle p \rangle}{\partial x_i} - G_{ij} \Omega (U_i - \tilde{U}_i(t)) dt + (C_0 k \Omega)^{1/2} dW_i, \quad (2.3)$$

where p is the pressure,

$$\Omega \equiv C_\Omega \frac{\langle \rho \omega | \omega \geq \tilde{\omega} \rangle}{\langle \rho \rangle}, \quad (2.4)$$

is the conditional Favre averaged turbulence frequency and

$$k = \frac{1}{2} \widetilde{u_i u_i} \quad (2.5)$$

is the turbulent kinetic energy. Note that the Favre averaging is equivalent to the Reynolds averaging for inert flows. The conditioning in Eq. 2.4 excludes the particles with turbulent frequency* less than mean turbulent frequency, that is, $\omega < \tilde{\omega}$, in evaluating the conditional mean turbulent frequency Ω to approximate the assumption that the rate of turbulent processes in the intermittent regions is represented by the turbulent particles better than the average of turbulent and non-turbulent particles [36]. The fluctuating velocity is defined as $\mathbf{u} = \mathbf{U} - \tilde{\mathbf{U}}$, where $\tilde{\mathbf{U}}$ is the Favre averaged mean velocity. Diffusion in velocity space is represented as a three-dimensional Wiener process

$\mathbf{W}(t)$, where ${}^1 dW_i(t) = W_i(t+dt) - W_i(t)$ is normally distributed with $\langle dW_i(t) \rangle = 0$ and $\langle dW_i(t)dW_j(t) \rangle = dt\delta_{ij}$. In Eq. 2.3, the second order tensor G_{ij} is usually specified such that the corresponding PDF model becomes equivalent to a Reynolds stress model at the second moment closure level [26, 27] and it can be written in the most general form as

$$G_{ij} \equiv \Omega(\alpha_1\delta_{ij} + \alpha_2b_{ij} + \alpha_3b_{ij}^2) + \mathbf{H}_{ijkl} \frac{\partial \tilde{U}_k}{\partial x_l}, \quad (2.6)$$

where the fourth-order tensor \mathbf{H} is

$$\begin{aligned} \mathbf{H}_{ijkl} = & \beta_1\delta_{ij}\delta_{kl} + \beta_2\delta_{ik}\delta_{jl} + \beta_3\delta_{il}\delta_{jk} + \gamma_1\delta_{ij}\delta_{kl} + \gamma_2\delta_{ik}b_{jl} + \gamma_3\delta_{il}b_{jk} \\ & + \gamma_4b_{ij}\delta_{kl} + \gamma_5b_{ik}\delta_{jl} + \gamma_6b_{il}\delta_{jk}. \end{aligned} \quad (2.7)$$

In Eq. 2.6, the normalized anisotropy tensor is defined as

$$b_{ij} = \frac{\langle u_i u_j \rangle}{\langle u_k u_k \rangle} - \frac{1}{3}\delta_{ij}. \quad (2.8)$$

The terms in $\alpha_{(i)}$ are the most general possible involving the Reynolds stress anisotropy b_{ij} alone, while the term \mathbf{H} is linear both in the mean velocity gradients and in the anisotropy [27]. The model coefficients are selected based on the corresponding Reynolds stress model at the second moment closure level as discussed by Pope [26, 27]. The simplified Langevin model (SLM) is widely used as a velocity model in PDF

¹ See Eq. 2.10 for the details of turbulent frequency.

simulations and it is also used in the present study. In this model the coefficient α_1 is specified as

$$\alpha_1 = -\left(\frac{1}{2} + \frac{3}{4}C_0\right) \quad (2.9)$$

The other coefficients for the SLM velocity model are summarized in Table 2.1 and 2.2. Note that the SLM model is equivalent to the Rotta's model [29] at the second moment closure level. The generalized Langevin models are potentially better than the SLM model as they involve more physics but this is not usually realized for the same reason as the corresponding Reynolds stress models: The model coefficients are not optimized. This is a task that is deferred to be done in future studies.

2.2.2 Turbulent Frequency Model

Turbulent frequency model provides a turbulence time scale needed to close the equations for the velocity and mixing models. The stochastic model for turbulent frequency is given by [36]

$$d\omega(t) = -C_3(\omega - \tilde{\omega})\Omega dt - S_w\Omega\omega(t)dt + (2C_3C_4\tilde{\omega}\Omega\tilde{\omega}(t))^{1/2}dW, \quad (2.10)$$

where W is an independent Wiener process, and the source term S_w is defined as

$$S_w = C_{w2} - C_{w1} \frac{P}{k\Omega} \quad (2.11)$$

where C_{w1}, C_{w2}, C_3, C_4 are the model constants specified in Table 2.1 and

$P = -\langle u_i u_j \rangle \frac{\partial \langle U_i \rangle}{\partial x_j}$ is the turbulent production rate. Note that the Reynolds averaging

denoted by $\langle \cdot \rangle$ must be replaced with the Favre averaging in the definition of the turbulent production rate when a reacting flow case is considered.

| Constant | Value | Used in |
|----------------|--------|----------------------------|
| C_0 | 2.1 | SLM |
| C_Ω | 0.6893 | Definition of Ω |
| $C_{\omega 1}$ | 0.65 | Turbulence frequency model |
| $C_{\omega 2}$ | 0.9 | Turbulence frequency model |
| C_3 | 1.0 | Turbulence frequency model |
| C_4 | 1.0 | Turbulence frequency model |
| C_ϕ | 2.0 | IEM mixing model |

Table 2.1: Model constants.

| Coefficients | α_1 | α_2 | α_3 | β_1 | β_2 | β_3 | $\gamma_{1,2,3,4,5,6}$ |
|--------------|--|------------|------------|-----------|-----------|-----------|------------------------|
| SLM | $-\left(\frac{1}{2} + \frac{3}{4}C_0\right)$ | 0 | 0 | 0 | 0 | 0 | 0 |

Table 2.2: The model constants for the SLM model.

2.2.3 Chemistry and Mixing Models

Although the case studied here is non-reacting so that there is no need for the chemistry and mixing model, they are described here briefly for completeness. A simple flamelet model is usually used in order to facilitate extensive computational simulations. In this model, the thermochemical state is characterized solely by the mixture fraction defined as

$$\xi = \frac{Z_i - Z_{i2}}{Z_{i1} - Z_{i2}}, \quad (2.12)$$

where the subscripts 1 and 2 denote the fuel and oxidizers, respectively, and Z_i is the mass fraction of the element i . Mixing models are needed to close the molecular diffusion terms in Eq. (2.2). There are several mixing models available but the simplest one is probably the interaction by exchange with the mean (IEM) model [6]. In the IEM model, the compositions evolve by

$$d\phi(t) = -\frac{1}{2}C_\phi\Omega(\phi(t) - \tilde{\phi})dt, \quad (2.13)$$

where C_ϕ is the model constant specified in Table 2.1. Note that $\phi = \xi$ when a simple flamelet model is used. Note that there must be a source term on the right hand side of Eq. 2.13 when a detailed chemistry model is used to account for the species formation or destruction due to chemical reactions. The chemical source term is usually highly nonlinear and causes major difficulty in conventional Reynolds averaged models while it appears to be in closed form in the PDF method. Note that LES method faces with the same difficulty about the nonlinear chemical reaction terms as the RANS models since chemical reactions occur at small scales which need to be modeled in LES. Therefore arbitrarily nonlinear chemical reactions are handled by the PDF method naturally without requiring any modeling assumptions. In fact, this unique feature enables the PDF method to correctly model the turbulence chemistry interactions. In particular, Xu and Pope [37] showed the local extinction and reignition processes are resolved correctly by the PDF method.

2.2.4 Modeled Joint PDF Evolution Equation

The modeled mass-weighted JPDF of velocity, turbulent frequency, and composition is defined as

$$\langle \rho \rangle \tilde{f}(\mathbf{V}, \psi, \theta; \mathbf{x}, t) = \rho(\psi) \langle \delta(\mathbf{U} - \mathbf{V}) \delta(\psi - \phi) \delta(\theta - \omega) \rangle. \quad (2.14)$$

The transport equation for $\tilde{f}(\mathbf{V}, \psi, \theta; \mathbf{x}, t)$ is derived from Eq. 2.3, 2.10 and 2.13 and the advection equation $\frac{d\mathbf{X}}{dt} = \tilde{\mathbf{U}} + \mathbf{u}$ using standard techniques as discussed Pope [25] and is given by

$$\begin{aligned} \frac{1}{\langle \rho \rangle} \frac{\partial (\langle \rho \rangle \tilde{f})}{\partial t} = & -\frac{V_i}{\langle \rho \rangle} \frac{\partial}{\partial x_i} (\langle \rho \rangle \tilde{f}) + \frac{\partial \langle \rho \rangle}{\partial x_i} \frac{\partial \tilde{f}}{\partial V_i} + G_{ij} \Omega \frac{\partial}{\partial V_j} [\tilde{f} (V_i - \tilde{U}_i)] \\ & + \frac{1}{2} C_0 k \Omega \frac{\partial^2 \tilde{f}}{\partial V_i \partial V_i} + \Omega \frac{\partial}{\partial \theta} (\tilde{f} \theta S_w) + C_3 \Omega \frac{\partial}{\partial \theta} [\tilde{f} (\theta - \tilde{w})] + C_3 C_4 \Omega \tilde{w} \frac{\partial^2}{\partial \theta^2} (\tilde{f} \theta) \\ & - \frac{\partial}{\partial \psi_a} [\tilde{f} S_a] + \frac{1}{2} C_\phi \Omega \frac{\partial}{\partial \psi_a} [\tilde{f} (\psi_a - \phi_a)] \end{aligned} \quad (2.15)$$

As can be seen in Eq. (2.15), \tilde{f} evolves in a high dimensional space, e.g., for a 3D flow it evolves in $(8 + n_s)$ dimensional space, where n_s is the number of compositions. Therefore it is not feasible to solve this equation using conventional numerical methods such as finite-difference or finite-volume techniques since the computational cost increases exponentially with the dimension of the equation in these methods. The only remaining alternative is the Monte Carlo method in which the computational cost increases only linearly with the dimensions except for the special dimensions and time. Although there exist Eulerian implementations of the Monte Carlo method for the PDF equations, the preferred solution method is the Lagrangian particle method [27].

2.3 Equations Solved by the Hybrid Method

The modeled PDF evolution equation is solved using the consistent hybrid FV/particle-based Monte Carlo method [22, 32]. All the equations solved by the hybrid method are

derived directly from modeled JPDF equation i.e., Eq. 2.15, and are thus fully consistent at the level of equations. The equations solved by the FV method and particle methods are briefly described here.

2.3.1 Mean Flow Equations Solved by the FV Method

In hybrid method FV solver is used to solve continuity and momentum equations. The mean mass conservation equation is obtained by integrating Eq. (2.15) over the entire sample space and is given by

$$\frac{\partial}{\partial t} \langle \rho \rangle + \frac{\partial}{\partial x_i} (\langle \rho \rangle \tilde{U}_i) = 0. \quad (2.16)$$

Similarly the mean momentum equations are obtained from Eq. (2.15) as the first moments of the velocity components and are given by

$$\frac{\partial}{\partial t} (\langle \rho \rangle \tilde{U}_i) + \frac{\partial}{\partial x_j} (\langle \rho \rangle \tilde{U}_i \tilde{U}_j + \langle \rho \rangle \delta_{ij}) = - \frac{\partial}{\partial x_j} (\langle \rho \rangle \widetilde{u_i u_j}) \quad (2.17)$$

Note that the Reynolds stress terms appearing in Eq. (2.17) are provided by the particle method. Although the density is constant in the present non-reacting case, the mean density field is also extracted from the particles for the reacting cases and passed to the FV code as will be discussed in the next Chapter.

2.3.2 Equations Solved by the Particle Algorithm

A particle based Monte Carlo method is used to solve the joint PDF transport equation of fluctuating velocity, turbulent frequency and compositions. The equations solved by the particle method are again derived directly from the modeled joint PDF evolution equation in the same way as described by Muradoglu et al. [22] and summarized here. A fluid particle moves with the local flow velocity, i.e.,

$$\frac{dX_i(t)}{dt} = \tilde{U}_i(t) + u_i(t). \quad (2.18)$$

The fluctuating velocity evolves by

$$du_i(t) = \frac{1}{\langle \rho \rangle} \frac{\partial \langle \rho \widetilde{u_i u_j} \rangle}{\partial x_j} dt - u_j \frac{\partial \tilde{U}_i}{\partial x_j} dt - G_{ij} \Omega_{ij}(t) dt + (C_0 k \Omega)^{1/2} dW_i \quad (2.19)$$

Finally the turbulent frequency and the compositions evolve by Eq. 2.10 and 2.13, respectively.

The mean velocity needed in the particle evolution equations are computed by the FV algorithm and passed to the particle code. The mean velocity field is then interpolated onto particle using the interpolation scheme developed by Jenny et al. [13]. The particle fields used in the equations solved by particle and FV algorithms are extracted from the particles using cloud-in-cell method [7]. It is emphasized here that the bias error is mainly caused by the statistical fluctuations in the mean fields used in particle evolution equations [7]. However, it has been demonstrated that the bias error is virtually eliminated by the hybrid algorithms [13, 22] due to the fact that the mean velocity field is computed by the FV method and it is therefore smooth.

Chapter 3

NUMERICAL METHOD

The PDF model equations have been described in the previous chapter. In this chapter, the hybrid FV/particle method is presented. Firstly the FV and particle algorithms are described separately and then the coupled FV/particle method is discussed. Since the present hybrid method is essentially the same as that of Muradoglu et al. [22], the general methodology is briefly discussed for completeness and emphasis is placed on the FV solver and on the associated coupling issues. Finally the new hybrid algorithm is applied to the non-reacting and reacting swirling bluff-body flows in order to demonstrate its numerical accuracy and robustness.

3.1 Finite Volume Scheme

The FV algorithm is essentially based on the cell-centered finite-volume scheme implemented in *caffa* code [24]. The code has been downloaded from the Internet and adopted to solve the mean flow equations, i.e., Eqs. (2.16) and (2.17). The method is based on the SIMPLE algorithm [4] and is second order accurate in space. Although the FV solver has both the steady and unsteady versions, only the steady version is used in the present study. Note that the method is also second order accurate in time when it is

used in the time-accurate mode. The axisymmetric equations and the FV algorithm is described below.

3.1.1 Axi-Symmetric Equations

Axi-symmetric flows are three-dimensional with respect to Cartesian coordinates, i.e., the velocity components are functions of all three coordinates, but they are only two-dimensional in a cylindrical coordinate system (all derivatives with respect to the circumferential direction are zero and all three velocity components are functions of only the axial and radial coordinates).

Assuming a statistically axisymmetric flows, the Favre averaged conservation equations for mass and momentum are given in a cylindrical coordinate system as

$$\frac{\partial \langle \rho \tilde{u}_z \rangle}{\partial z} + \frac{1}{r} \frac{\partial \langle \rho \tilde{u}_r \rangle}{\partial r} = 0, \quad (3.1)$$

$$\begin{aligned} \frac{\partial \langle \rho \tilde{u}_r \tilde{u}_r \rangle}{\partial r} + \frac{\partial \langle \rho \tilde{u}_r \tilde{u}_r \rangle}{\partial r} + \frac{\partial \langle \rho \tilde{u}_r \tilde{u}_z \rangle}{\partial z} + \frac{\partial \langle \rho \tilde{u}_r \tilde{u}_z \rangle}{\partial z} \\ = \langle \rho \tilde{u}_\theta \tilde{u}_\theta \rangle + \langle \rho \tilde{u}_\theta \tilde{u}_\theta \rangle - \frac{\partial \langle r(p) \rangle}{\partial r} \end{aligned} \quad (3.2)$$

$$\begin{aligned} \frac{\partial \langle \rho \tilde{u}_r \tilde{u}_\theta \rangle}{\partial r} + \frac{\partial \langle \rho \tilde{u}_r \tilde{u}_\theta \rangle}{\partial r} + \frac{\partial \langle \rho \tilde{u}_\theta \tilde{u}_z \rangle}{\partial z} + \frac{\partial \langle \rho \tilde{u}_\theta \tilde{u}_z \rangle}{\partial z} \\ = -\langle \rho \tilde{u}_r \tilde{u}_\theta \rangle - \langle \rho \tilde{u}_r \tilde{u}_\theta \rangle \end{aligned} \quad (3.3)$$

$$\frac{\partial \langle \rho \tilde{u}_r \tilde{u}_z \rangle}{\partial r} + \frac{\partial \langle \rho \tilde{u}_r \tilde{u}_z \rangle}{\partial r} + \frac{\partial \langle \rho \tilde{u}_z \tilde{u}_z \rangle}{\partial z} + \frac{\partial \langle \rho \tilde{u}_z \tilde{u}_z \rangle}{\partial z} = -\frac{\partial \langle r(p) \rangle}{\partial z} \quad (3.4)$$

where r and z are the coordinates in the radial and axial directions, respectively. The quantities with subscripts r and z denote the obvious quantities.

3.1.2 Finite Volume Method

The Favre-averaged flow equations are solved using a FV method. The Reynolds stress terms that appear in the mean momentum equations are supplied by the particle method. The present FV scheme is essentially based on the SIMPLE algorithm and the code is downloaded from the internet and adopted to the hybrid algorithm as discussed by Eren [10]. The basic idea is explained here and details can be found in Peric [24]. The mean mass conservation and the Favre-averaged Navier-Stokes equations can be integrated over the control volume $abcd$ as sketched in Fig. 3.1 and using the Stokes' theorem, the mean flow equations can be expressed in the integral form. The surface integrals are splitted into four CV face integrals. Approximation of the convective and diffusive fluxes and the source terms are considered on CV face 'e' in the sketch in Fig. 3.1. The other faces are treated in the same way, and the results can be obtained by index substitution. This FV method is equivalent to the second order central differences on a regular Cartesian grid. Fluxes are approximated such that the quantities at a CV face center represent the mean

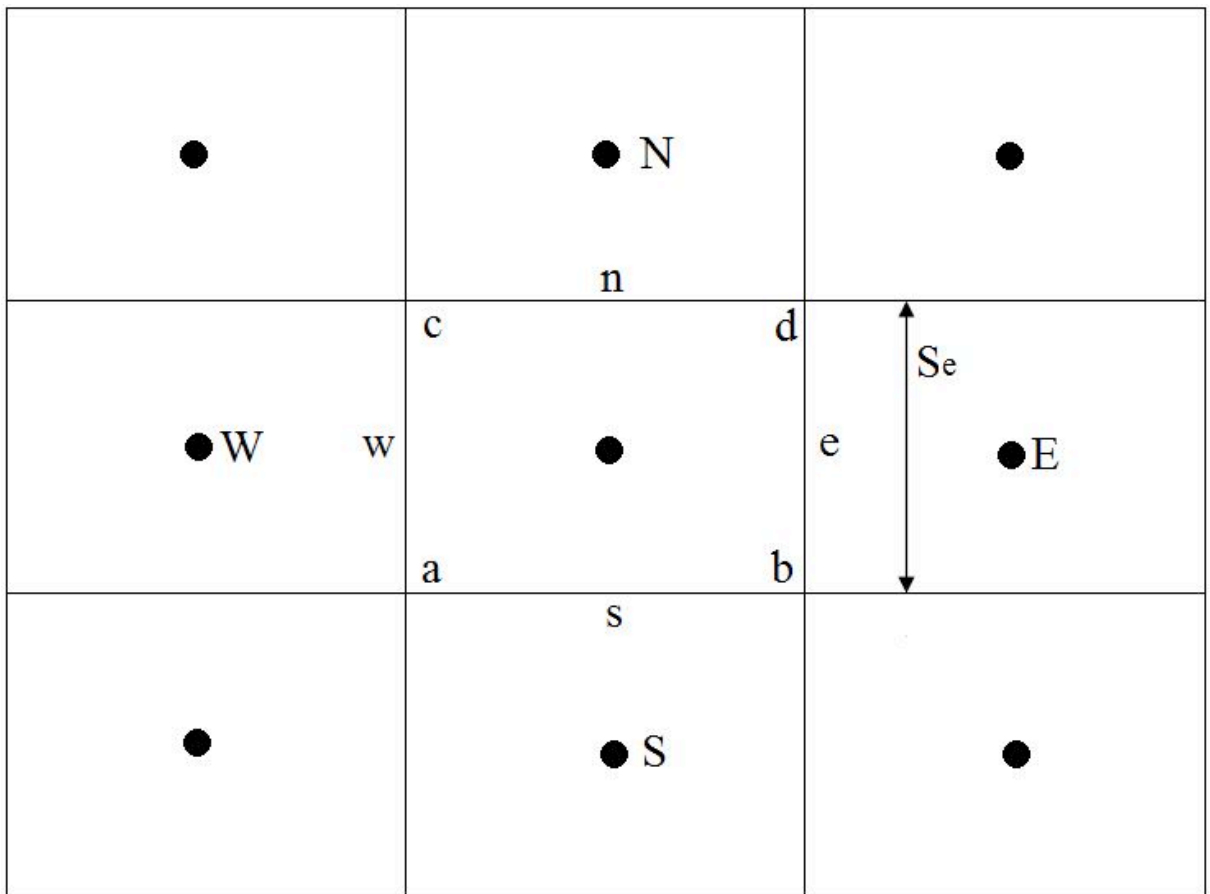


Figure 3.1: A collocated FV grid. Mean fields are stored in the center of the cells. E, W, S, N denotes the centers of the Eastern, Western, Southern, and Northern cells, respectively. Cell faces are denoted by e, w, s, n for Eastern, Western, Southern and Northern cell faces, respectively. Length of the eastern cell face is denoted as S_e .

values over the face. On the m^{th} outer iteration, all nonlinear terms are approximated by a product of an 'old' (from the preceding outer iteration) and a 'new' value. Thus, in discretizing the momentum equations, the mass flux through each CV face is evaluated using the existing velocity field and is assumed to be known, i.e.,

$$\dot{m}_e^m = \int_{abcd} \langle \rho \rangle \tilde{U}_i n_i dS \approx (\langle \rho \rangle \tilde{U}_i)_e^{m-1} S_e \quad (3.5)$$

where S_e is the area of eastern face and U_e is the velocity component in the direction of normal vector. Note that, unless specified otherwise, all the quantities are written for the m^{th} outer iteration and the superscript m is dropped in the remainder of this section. Mass fluxes at the faces of the CVs are obtained by interpolation. For instance, the mass flux on the east CV face is calculated as:

$$\dot{m}_e = \frac{1}{2}(\dot{m}_P + \dot{m}_E). \quad (3.6)$$

Mass fluxes from other faces can be calculated by substituting indices. The convective flux through ‘e’ face is:

$$\int_{abcd} \langle \rho \rangle \tilde{U}_i \tilde{U}_j n_j dS \approx (\tilde{M}_e \tilde{U}_i)_e \quad (3.7)$$

The CV face value of \tilde{U}_i used in the above expression can be found using simple linear interpolation central difference scheme (CDS), but some iterative solvers fail to converge when applied to algebraic equation systems derived from central difference approximations of convective fluxes because the matrices may not be diagonally dominant [24]. Thus, these equations are solved using deferred correction [24] approach in which the flux is expressed as:

$$F_{i,e}^c = \dot{m}_e \tilde{U}_{i,e}^{UDS} + \dot{m}_e (\tilde{U}_{i,e}^{CDS} - \tilde{U}_{i,e}^{UDS})^{m-1}, \quad (3.8)$$

where superscript CDS and UDS denote approximation by central and upwind differences, respectively. The outward unit normal vector at CV face ‘e’ is I , and thus the turbulent fluxes are calculated as:

$$Q_{i,e}^T = - \int_{abcd} \widetilde{u_i u_x} dS \approx (\widetilde{u_i u_x})_e S_e \quad (3.9)$$

The pressure terms are approximated by:

$$Q_u^p = - \int_S p_i \cdot n dS \approx -(p_E S_E - p_P S_P)^{m-1} \quad (3.10)$$

The approximation to the complete momentum equation is:

$$F_i^c = Q_i^T + Q_i^p + Q_i^r, \quad (3.11)$$

Then the total fluxes for the CV is given by

$$F^c = F_e^c + F_w^c + F_n^c + F_s^c \quad (3.12)$$

When the approximation for the convective fluxes are substituted into Eq. (3.11), the following form of algebraic equation is obtained:

$$A_p^u \tilde{U}_{i,p} + \sum_l A_l^u \tilde{U}_{i,l} = Q_p^u, \quad l = E, W, N, S. \quad (3.13)$$

The coefficients depend on the approximation used; for the UDS approximations applied for convective fluxes, the coefficient for the convective flux on face 'e' the equation is:

$$A_E^u = \min(\dot{m}_e^u, 0). \quad (3.14)$$

The corresponding coefficients for other faces can be obtained by changing the indices. Similarly

$$A_p^u = - \sum_l A_l^u, \quad l = E, W, N, S. \quad (3.15)$$

The source term Q_p^u contains the pressure and Reynolds stress terms but also the portion of convective fluxes resulting from deferred correction:

$$Q_p^u = Q_u^p + Q_u^b + Q_u^c + Q_u^r, \quad (3.16)$$

where

$$Q_{\tilde{U}_i}^c = \left[\left(F_{\tilde{U}_i}^c \right)^{UDS} - \left(F_{\tilde{U}_i}^c \right)^{CDS} \right]^{m-1} \quad (3.17)$$

The convective source is calculated using the velocities from the previous outer iteration $m-1$. Note that solution for the above momentum equation does not give the right velocity field and needs to be corrected. Therefore, the SIMPLE algorithm of Caretto et al. [4] is employed.

3.1.3 SIMPLE Method

For convenience, in this subsection axial and radial components of \tilde{U}_i will be denoted as u and v , respectively. The linearized momentum equations, i.e., Eq. 3.13 are solved with sequential solution method [24] using ‘old’ mass fluxes and the pressure from the previous outer iteration. This produces new velocities u^* and v^* which do not necessarily satisfy the continuity equation so:

$$\dot{m}_e^* + \dot{m}_w^* + \dot{m}_n^* + \dot{m}_s^* = \Delta \dot{m}_p^*, \quad (3.18)$$

where $\Delta \dot{m}_p^*$ is the residual. The velocity components u^* and v^* calculated from the momentum equations can be expressed as follows:

$$u_e^* = \tilde{u}_e^* - \frac{S_e}{A_p^u} (p_E - p_P)^{m-1}, \quad (3.19)$$

where \tilde{u}_e^* is shorthand notation for

$$\tilde{u}_e^* = \frac{Q_p^u - Q^p - \sum_l A_l^u u_l^*}{A_p}. \quad (3.20)$$

Analogously, v_n^* is expressed as:

$$v_n^* = \tilde{v}_n^* - \frac{S_n}{A_p^v} (p_N - p_P)^{m-1}, \quad (3.21)$$

The velocities u^* and v^* are corrected to enforce mass conservation through pressure correction. The corrected velocities $u^m = u^* + u'$ and $v^m = v^* + v'$ are enforced to satisfy linearized momentum equations by correcting the pressure, thus:

$$u_e^m = \tilde{u}_e^m - \frac{S_e}{A_p^u} (p_E - p_P)^m, \quad (3.22)$$

and

$$v_n^m = \tilde{v}_n^m - \frac{S_n}{A_p^v} (p_N - p_P)^m \quad (3.23)$$

where $p^m = p^{m-1} + p'$ is the new pressure. The relation between the velocity and pressure correction is obtained by subtracting Eq. (3.19) from Eq. (3.22):

$$u_e' = \tilde{u}_e' - \frac{S_e}{A_p^u} (p_E' - p_P'), \quad (3.24)$$

where

$$\tilde{u}_e' = \tilde{u}_e^m - \tilde{u}_e^* = \frac{\sum_l A_l^u u_l'}{A_p}. \quad (3.25)$$

Analogously,

$$v'_n = \tilde{v}'_n - \frac{S_n}{A_p^v} (p'_N - p'_P). \quad (3.26)$$

The velocities u^m and v^m are substituted into the expressions for mass fluxes to enforce continuity equation, i.e.,

$$(\rho S u')_e - (\rho S u')_w + (\rho S u')_n - (\rho S u')_s + \Delta \dot{m}_p^* = 0. \quad (3.27)$$

Finally, the above expressions for u' and v' are substituted into the continuity equation leading to the pressure correction equation:

$$A_p^p p'_P + \sum_l A_l^p p'_l = -\Delta \dot{m}_p^* - \Delta \dot{m}'_p, \quad (3.28)$$

where the coefficients are:

$$\begin{aligned} A_E^p &= -\left(\frac{\rho S^2}{A_p^u}\right)_e, \quad A_W^p = -\left(\frac{\rho S^2}{A_p^u}\right)_w, & A_S^p &= -\left(\frac{\rho S^2}{A_p^v}\right)_s, \\ A_S^p &= -\left(\frac{\rho S^2}{A_p^v}\right)_s, \quad A_p^p = -\sum_l A_l^p, & l &= E, W, N, S. \end{aligned} \quad (3.29)$$

The term $\Delta \dot{m}'_p$ is analogous to $\Delta \dot{m}_p^*$, with \tilde{u}' and \tilde{v}' replacing \tilde{u}^* and \tilde{v}^* . Since the velocity corrections are not known prior to the solution of the pressure-correction equation, this term is neglected having the SIMPLE algorithm [24]. Other alternatives are the SIMPLER and the PISO [24]. After the pressure-correction equation is solved, the velocities and pressure are corrected. The corrected velocities satisfy the continuity equation to the accuracy with which the pressure-correction equation is solved. However, they do not satisfy the non-linear momentum equation, so another outer iteration is

needed. When both the continuity and momentum equations are satisfied to the desired accuracy, convergence is achieved.

3.2. Particle Method

The particle method is described in the context of the hybrid method and is essentially based on that of Muradoglu et al. [22]. In this approach, the fluid particles are represented by an ensemble of notional particles distributed in the physical space. Each particle has the intrinsic properties of mass m^* , position \mathbf{X}^* , fluctuating velocity \mathbf{u}^* and compositions ϕ^* . The particle properties are denoted by superscript $*$ throughout the thesis unless specified otherwise. A non-uniform Cartesian grid is cast on the computational domain in order to estimate the particle fields needed in the particle evolution equations and the equations solved by the FV algorithm. The grid is also used to interpolate the particle and FV mean fields onto the particles. Note that the same grid is used in this study both for the particle and FV algorithms. The particle fields such as $\langle \rho \rangle^*$ and $(\widetilde{u_i u_j})^*$ are extracted from the particle properties using a cloud-in-cell (CIC) method [7]. The mean quantities needed in the particle evolution equations are interpolated from the nodal values of the corresponding FV or particle fields using bilinear splines. The spatial derivatives of the mean quantities that appear in the particle evolution equations are first evaluated at the nodes using second order central differences and then interpolated onto the particle locations.

The particle positions evolve according to

$$\frac{dX_i^*(t)}{dt} = \tilde{U}_i^*(t) + u_i^*(t), \quad (3.30)$$

where $\tilde{U}_i^*(t)$ is the mean velocity interpolated from the FV field onto the particle location. The fluctuating velocity evolves by

$$du_i(t) = \frac{1}{\langle \rho \rangle} \frac{\partial \langle \rho \widetilde{u}_i \widetilde{u}_j \rangle}{\partial x_j} dt - u_j \frac{\partial \widetilde{U}_i}{\partial x_j} dt - G_{ij} \Omega_{ij}(t) dt + (C_0 k \Omega)^{1/2} dW_i \quad (3.31)$$

and turbulence frequency and compositions by

$$dw^*(t) = -C_3 (w^* - \tilde{w}) \Omega dt - S_w \Omega w^*(t) dt + (2C_3 C_4 \tilde{w} \Omega w^*(t))^{1/2} dW, \quad (3.32)$$

and

$$d\phi^*(t) = -\frac{1}{2} C_\phi \Omega (\phi^*(t) - \tilde{\phi}) dt, \quad (3.33)$$

respectively. The particle equations 3.30, 3.31, 3.32 and 3.33 are integrated forward in time using the explicit second order scheme as described by Muradoglu et al. [9].

3.3 Coupled FV/Particle Algorithm

The FV and particle methods are periodically used to solve their respective equations. Each period is called an “outer” iteration that consists of FV and particle “inner” iterations. The FV and particle algorithms are coupled in a semi loosely coupled fashion [13], i.e., the FV code is run until it reaches a pseudo steady state while the particle code is run for a single time step to complete an outer iteration. The mean density and the Favre averaged Reynolds stresses are supplied to the FV code by the particle algorithm which, in turn, gets the mean velocity and pressure fields from the FV solver. Although it can be easily adopted to perform time accurate computations, the present implementation is designed to treat only the statistically stationary flows. Therefore time-averaging is performed to reduce statistical error both in the particle and FV fields. Following Muradoglu et al. [9], for a mean field Q , the time-averaged mean Q_{TA} is evaluated as follows

$$Q_{TA}^k = \left(1 - \frac{1}{N_{TA}}\right) Q_{TA}^{k-1} + \frac{1}{N_{TA}} Q_{TA}^k, \quad (3.34)$$

where k denotes the k^{th} particle time step and N_{TA} is the time-averaging factor to be specified. The time-averaging factors for the FV fields used in the FV algorithm, for the particle fields used in the FV algorithm and for the particle fields used in the particle algorithm are denoted by $N_{TA}^{FV}, N_{TA}^{P2FV}, N_{TA}^{P2P}$, respectively. Throughout this thesis, unless specified otherwise, the time-averaging factors are fixed at 5, 10 for $N_{TA}^{FV}, N_{TA}^{P2FV}$ and 20 for N_{TA}^{P2P} in the initial phase of calculations and is increased to 500 when statistically steady state is approached.

As mentioned before, although the present hybrid method is completely consistent at the level of governing equations, a full consistency at the numerical solution level may not be achieved due to accumulation of numerical error. Therefore correction algorithms are needed to enforce the full consistency at the numerical level. Since the density field is supplied to the FV algorithm by the particle code, there are only two independent consistency conditions in the present hybrid method given by

$$\tilde{u}^* = 0. \quad (3.35)$$

and

$$\langle \rho \rangle_p = q \quad (3.36)$$

where q is the particle mass density [22]. The velocity and position correction algorithms are used to enforce the consistency conditions given by Eqs. 3.35 and 3.36, respectively. The correction algorithms are the same as those described by Muradoglu et al. [22].

Chapter 4

RESULTS AND DISCUSSIONS

4.1 Introduction

The velocity-turbulence frequency joint PDF method is applied to study the non-reacting swirling bluff body flow studied experimentally by Masri et al. [1]. The bluff body stabilized swirl combustors are widely used in industrial applications due to their enhanced mixing characteristics, improved flame stability and ease of combustion control [10]. Besides their practical significance, Sydney Swirl burner studied here provides an excellent but challenging test case for the numerical solution algorithms and turbulence models because of its simple and well defined initial and boundary conditions, and its ability to maintain the flame stabilization for a wide range of inlet flow conditions with a complex recirculation zone [1]. The swirling flow studied here is among the target flows selected for the assessment of performance of the turbulence and combustion models in TNF workshops. As mentioned before, this is the first step towards modelling of the swirling flames and combustors.

4.2 Experimental Setup

The experimental setup used by Masri et al. [1] is first described here. A schematic of the Sydney swirl burner is shown in Fig. 4.1 where the axisymmetric computational domain

is also sketched. The swirl burner is essentially an extension to the bluff-body burner developed by the same group. Swirl is induced aerodynamically into the primary (axial) air stream at a distance of 300 mm upstream of the burner exit. This occurs via tangential (air) swirl ports (7 mm diameter) that are inclined at 15° upwards (off the horizontal plane). Two diametrically opposed ports, also located on the periphery of the burner, but ahead of the tangential inlets, supply the axial streams of the air [1]. As can be seen in Fig. 4.1, a fuel jet is ejected through a 3.6 mm-diameter nozzle centred in a 50 mm-diameter cylindrical bluff-body surrounded by a 5 mm wide annulus which supplies the swirling air stream. For the sake of well-defined boundary conditions, the burner is placed in a square wind tunnel with an exit cross section of $130 \times 130 \text{ mm}^2$. Further details about the setup can be found online [20] and in the original publication by Masri et al. [1].

In Sydney swirl burner, there are four main parameters that determine the flow behaviour and the flame characteristics. These are the bulk velocity of the fuel jet U_j , the bulk axial and tangential velocity in the primary air supply denoted by U_c and W_c , respectively, as well as the velocity of the coflow in the wind tunnel, U_e . The level of swirl is characterised by the geometric swirl number S_g defined by Masri et al. [1] as the ratio of bulk tangential to primary axial air velocities ($S_g = W_c/U_c$).

Masri et al. [1] investigated both the non-reacting and reacting swirling bluff-body flows in various flow conditions. The non-reacting cases are important in order to assess the performance of the turbulence models separately from the chemistry models. In addition, it allows to test the performance of the numerical solution algorithm and to optimize the numerical parameters such as relaxation factors. Once the turbulence model and solution algorithm are optimized for the non-reacting case, then we can study the reacting cases concentration on the chemistry models and related issues. In the present study, one particular non-reacting case, i.e., N16S159 cases in Masri et al. [1] is selected

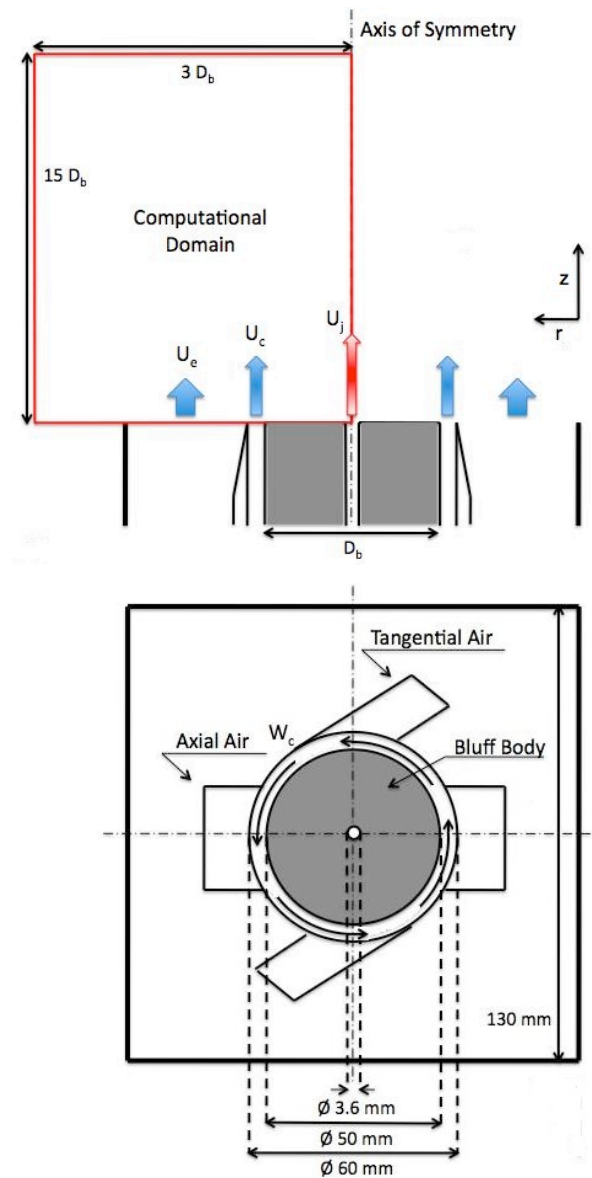


Figure 4.1: Sketch of the swirling bluff-body flows. The diameter of the bluff-body is denoted by D_b . Axial and radial lengths of the computational domain are set to $15D_b$ and $3D_b$, respectively. The boundaries of the computational domain are shown in red.

as test case. The bulk axial velocity is linearly proportional to the mass flow rate of air through the annulus and is set to $U_c = 16.3$ m/s in the case of N16S159. The tangential component of the velocity in the annulus (swirl) is set to $W_c = 25.9$ m/s. The secondary (co-flow) air stream generated in the wind tunnel is fixed at $U_e = 20$ m/s. The jet velocity through the central tube of diameter 3.6 mm is set to $U_j = 66$ m/s. By changing the relative magnitudes of the tangential and axial airflow rates, the swirl number, which is $S_g = 1.59$ in the flow case studied in this thesis, can be varied. Table 4.1 outlines the flow conditions investigated in this thesis.

| Flow Case | U_c (m/s) | W_c (m/s) | U_j (m/s) | U_e (m/s) | S_g |
|-----------|-------------|-------------|-------------|-------------|-------|
| N16S159 | 16.3 | 25.9 | 66 | 20 | 1.59 |

Table 4.1: Investigated flow conditions.

In Figure 4.2, 3D geometry of the Sydney swirl burner and the helical characteristics of the swirling flow through the annulus as well as the coflow air stream through the wind tunnel and axial fuel jet are sketched to help visualizing the turbulent flow studied here. Note that the outer boundary is sufficiently far from the bluff-body and swirling annulus so that the flow is considered as unconfined in the present study. This also allows us to model the flow as statistically axisymmetric.

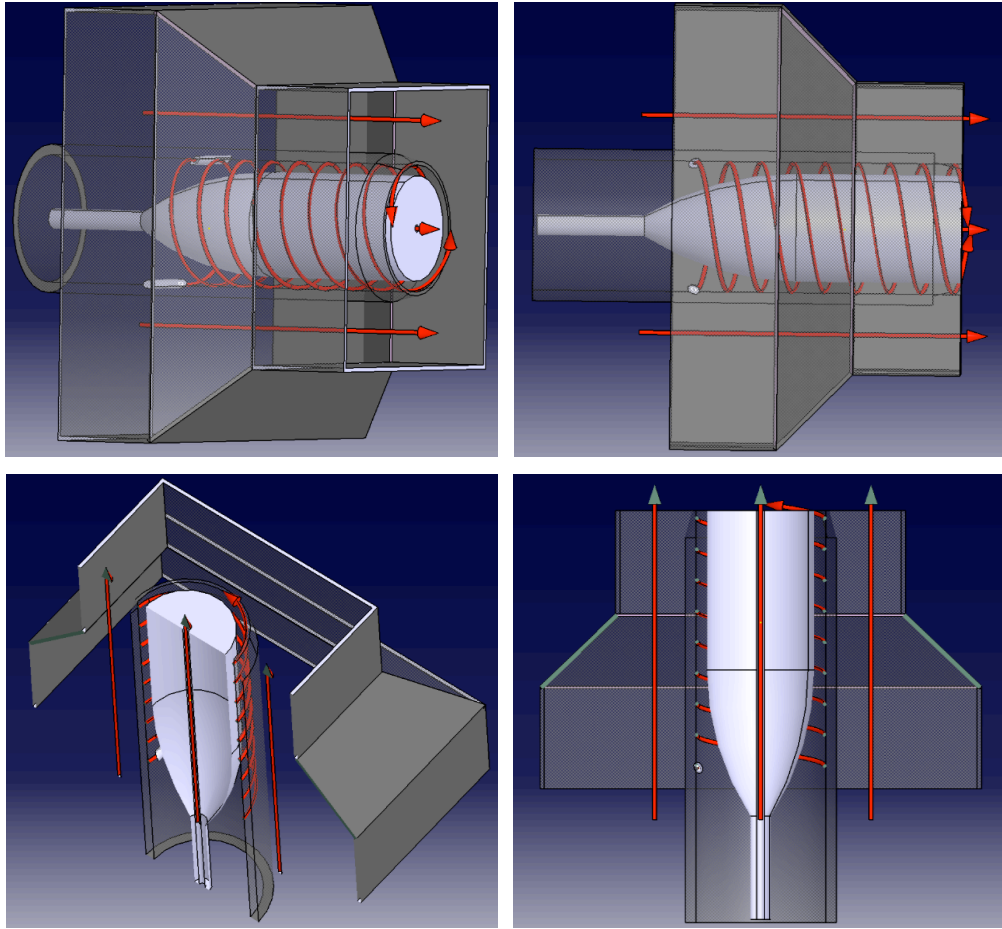


Figure 4.2: 3D technical drawings of the Sydney Swirl Burner from different angles.

4.3 Computational Domain and Computational Grid

As sketched in Fig. 4.1, a rectangular computational domain with 0.75 m ($15D_b$) in the axial direction and 0.15 m ($3D_b$) in the radial direction is selected, where D_b stands for the diameter of the bluff-body. Inlet boundary conditions are specified at $z = 0$. The radius of the fuel jet is $R_j = 0.0018$ m and the radius of the bluff-body is $R_b = 0.025$ m. The outer boundary in the radial direction is located at $r = 0.15$ m.

A tensor-product two-dimensional Cartesian grid is employed in the present study. The computational grid is stretched in the jet region and also in the jet/bluff-body and bluff-body/co-flow shears layers as the flow properties are expected to change most rapidly in these regions. The computational grid is also stretched in the re-circulating region. Figure 4.3 shows a sample (coarse) computational grid used in this study with $n_z = 25$ and $n_r = 20$, where n_z and n_r are the number of cells in axial and radial directions, respectively. Some properties of the computational grids used in this thesis are summarized in Table 4.2. Note that the same computational grid is used both in the FV and particle codes for convenience although it is possible to use different grid sets if needed. Using the same grid set has an advantage especially in interpolating the mean velocity field onto particle. This interpolation must be done carefully in order to guarantee the mass conservation at discrete level as discussed by Jenny et al. [13] and recently by McDermott and Pope [21].

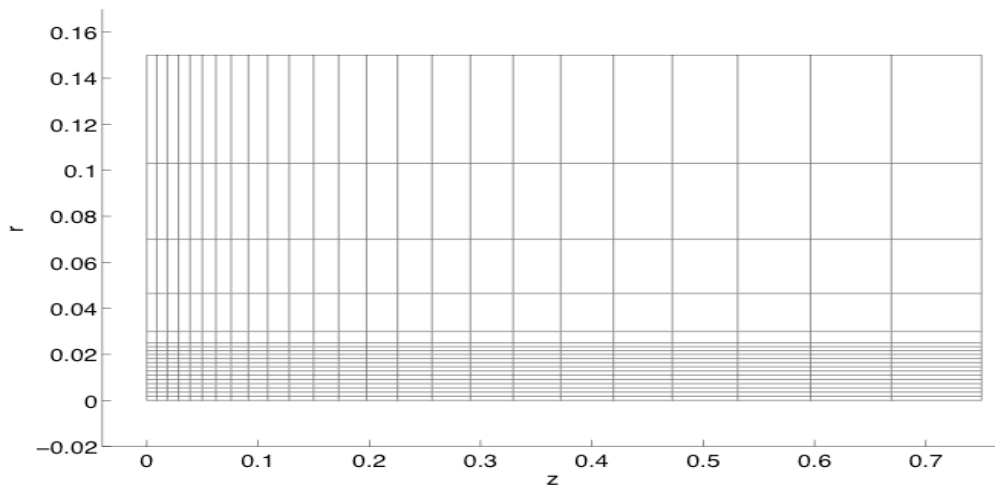


Figure 4.3: A coarse computational grid with number of grid parts in the axial and radial directions, $n_z = 25$ and $n_r = 20$, respectively.

| Grid | Region 1 | Region 2 | Region 3 |
|-----------|----------|----------|----------|
| 64 x 64 | 8 | 40 | 16 |
| 96 x 96 | 12 | 60 | 24 |
| 128 x 128 | 16 | 88 | 32 |
| 160 x 160 | 20 | 108 | 40 |

Table 4.2: Number of cells used in three regions in different grids. Region 1, 2 and 3 denote jet, bluff-body and co-flow regions, respectively.

4.4. Boundary Conditions

An important advantage of the present swirling bluff-body flow is its well-defined boundary and initial conditions. The geometry and the computational setup of the bluff-body flows are sketched in Fig. 4.1. The inlet and boundary conditions are the same as those used by Masri et al. [1] for the non-reacting case. A fully developed turbulent pipe flow is assumed in the jet region and variances of velocity are interpolated from the experimental data. Following Jenny et al. [13] and Muradoglu et al. [22], the mean turbulent shear stresses are calculated as

$$\overline{u_z u_r} = \rho_{12} (u_z^2 u_r^2)^{0.5} \quad (4.1)$$

where u_r and u_z are axial and radial components of the fluctuating velocity, $\rho_{12} = -0.4$ and $\rho_{12} = 0.5(z/R_j)$ in the coflow and jet regions, respectively. Particle fluctuating velocity components are specified so that they have zero mean at the inlet. Turbulent frequency at the inlet is specified using

$$\tilde{\omega} = \frac{P}{k} = -\frac{\widetilde{u_z u_r}}{k} \frac{\partial \tilde{U}}{\partial r} \quad (4.2)$$

where k is the turbulent kinetic energy and P is the mean turbulent energy production rate defined as $P = -\langle u_i u_j \rangle \frac{\partial \langle U_i \rangle}{\partial x_j}$. A perfect slip is assumed on the bluff-body since it is computationally costly to resolve the thin boundary layer on the bluff-body surface. The inlet boundary conditions are also used as initial conditions since we are only interested in the statically stationary solutions so the initial conditions are not important as long as a statistically steady state is reached. In the co-flow region the experimental data are used as the inlet conditions for the mean velocity fields including tangential velocity component. The experimental data are available from Internet [20]. Initially, the tangential velocity field is set to the primary inlet coflow air velocity in the entire computational domain. Density is set to the air density at the standard conditions. The outlet boundary conditions are set at $z = 0.75$ m. At the outlet, pressure is set to the atmospheric pressure, 1 atm. Particles leaving the computational domain at the outlet are simply eliminated. At the centreline, symmetry boundary conditions are applied both for FV solver and particle method. Particles crossing the centreline are reflected back into the computational domain.

4.5. Simulations

PDF simulations are now performed for the non-reacting swirling bluff-body flow case labelled as N16S159 by Masri et al. [5]. The consistent hybrid method is employed to solve the modelled velocity-turbulence frequency PDF evolution equation. Table 4.2 summarizes the flow conditions used in the simulations. The number of particles per cell is fixed at 50, which has been shown previously to be sufficient to reduce the associated

numerical error below 5% for this kind of flows [8]. Maximum outer iterations are set to 15 for the FV solver and 1 for the particle algorithm.

As mentioned before, the present hybrid algorithm is designed to simulate the statistically stationary flows. Therefore, the statistical stationarity is first examined for N16S159 case. For this purpose, the mean axial velocity and mean turbulent kinetic energy are monitored at six selected locations and are plotted as a function of particle time step in Fig. 4.4. As can be seen in this figure, the statistically stationary state is reached in about 2500 particle time steps.

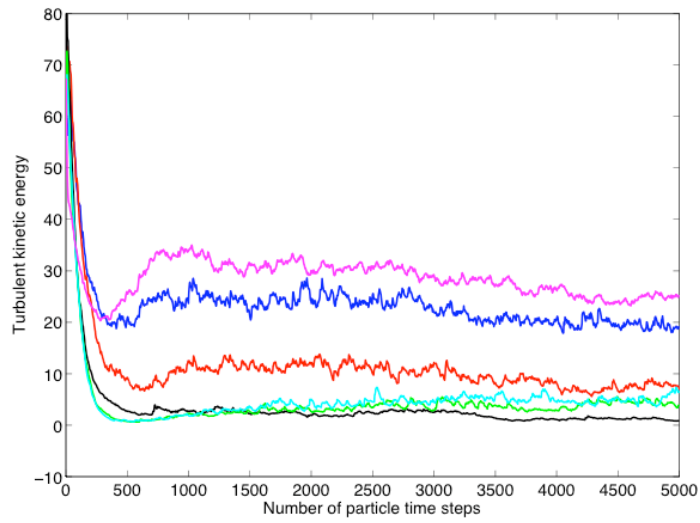
| | Axial Distance | Radial Distance |
|------------|----------------|--------------------------|
| Location 1 | $0.6 D_b$ | 0 |
| Location 2 | $0.6 D_b$ | R_j |
| Location 3 | $0.6 D_b$ | mid bluff-body = 13.4 mm |
| Location 4 | $1 D_b$ | 0 |
| Location 5 | $1 D_b$ | R_j |
| Location 6 | $1 D_b$ | mid bluff-body = 13.4 mm |

Table 4.3: Six selected locations in the downstream of the bluff-body to monitor the statistically steady state. $D_b = 50$ mm is bluff-body diameter and $R_j = 1.8$ mm is jet radius.

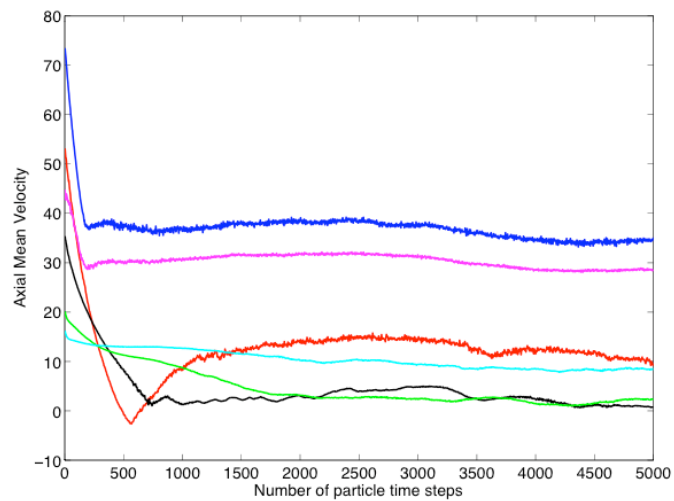
After showing the statistical stationarity of the hybrid method, the computed mean fields are now compared with the experimental data. The computations are performed

using a 64x64 grid. Note that the issue of grid convergence will be discussed below in this section. The mean axial and tangential velocity contours are first compared qualitatively in Figs. 4.5 and 4.6, respectively. These figures indicate reasonably good qualitative agreement between the computed and experimental results. Then the experimental and computed velocity vectors are plotted in Figs. 4.7a and 4.7b, respectively in order to show the flow field in the recirculation region. Again a good qualitative agreement is observed in the velocity vector plots. Finally the statistically stationary streamlines are plotted in Fig. 4.8 to show the overall flow structure of the recirculation zone behind the bluff-body. This plot shows that the recirculation zone is captured by the PDF simulations. However, it shows some indications for vortex shedding that has not been observed experimentally. In fact, similar results were also reported by Jenny et al. [14] for the non-reacting and non-swirling bluff-body flow case. The vortex shedding increases as the grid is refined as also observed by Jenny et al. [14]. Now the computed results are quantitatively compared with the experimental data in terms of mean quantities. For this purpose, the computed mean axial velocity profiles are compared with the experimental data in Figs. 4.9a and 4.9b at the axial locations of $z/D_b = 0.136, 0.2, 0.5, 0.6, 0.8, 1.2, 2.0$ and 2.5 . These figures indicate that there is reasonably good agreement between the computed and experimental mean axial velocity profiles especially near the bluff-body. Predicting the mean tangential velocity is of critical importance since it represents the effects of the swirl. The computed tangential mean velocity profiles are plotted in Fig. 4.10 and are compared with the experimental data. As can be seen in this figure, the computed tangential mean velocity profiles match well with experimental data indicating the accuracy of resolving the effects of the swirl. As can be seen in Figs.9 and 10, there is generally a reasonably good agreement between the computational and experimental results for all mean fields. Finally, the hybrid algorithm is applied to swirling non-reacting bluff-body flow using different grid sizes in order to

examine grid convergence. For this purpose, the profiles of mean axial and tangential velocities computed using 64x64, 96x96, 128x128 and 160x160 grids are plotted in Figs. 4.11(a, b) and 4.12(a, b), respectively. As can be seen in these Figures, the mean axial and tangential velocity fields are successfully resolved by different grid sizes. However, although the experimental and computational results are in a good agreement, a full grid convergence is not really achieved mainly due to the fact that a vortex shedding occurs on very fine grids as mentioned above. Note that similar vortex shedding was also observed in the PDF simulations performed for the non-swirling bluff-body flow [14].

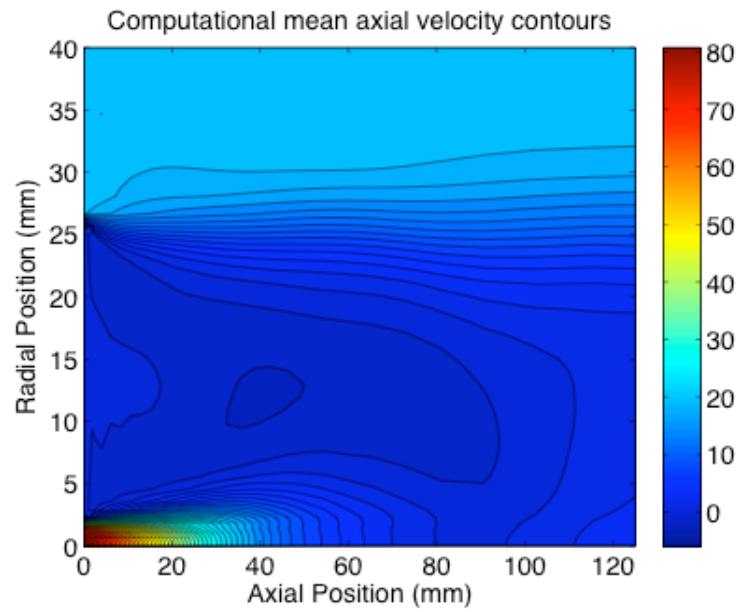


(a)

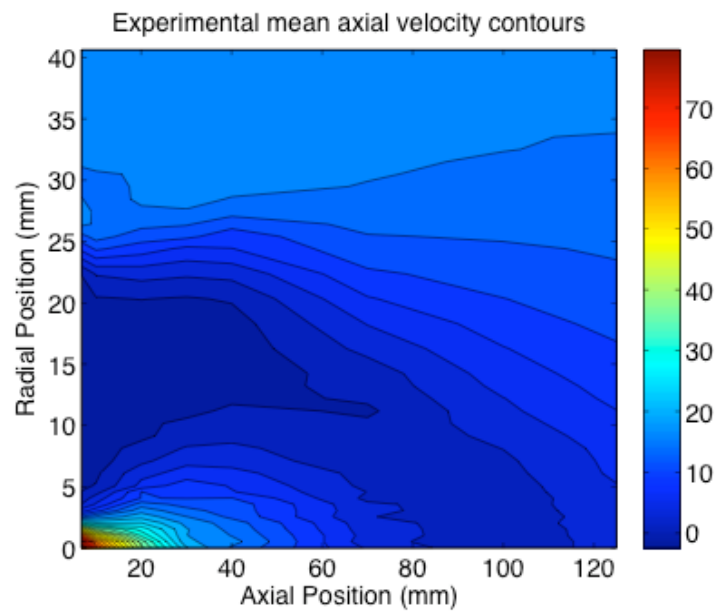


(b)

Figure 4.4: Convergence histories of (a) the mean turbulent kinetic energy and (b) the mean axial velocity for non-reacting swirling bluff-body flow.

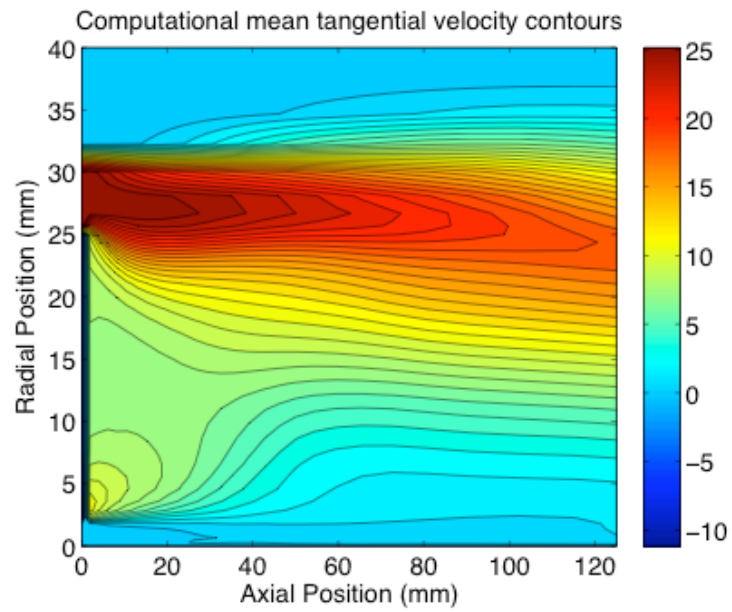


(a)

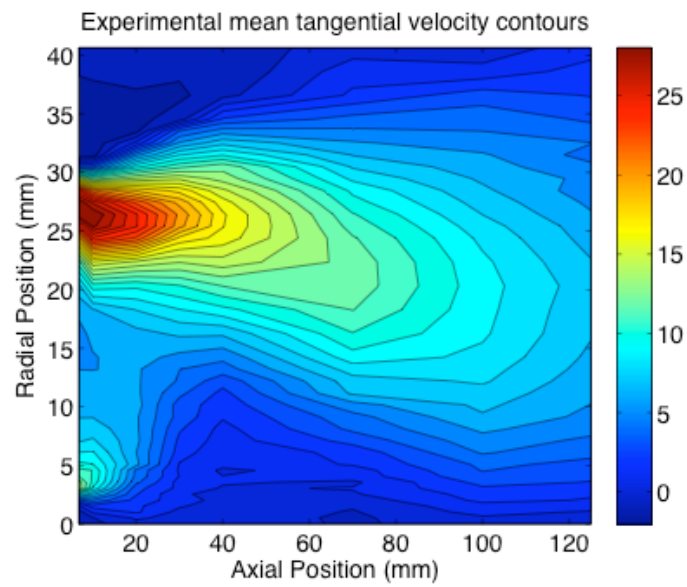


(b)

Figure 4.5: Mean axial velocity contour plots. (a) Computational (b) Experimental.

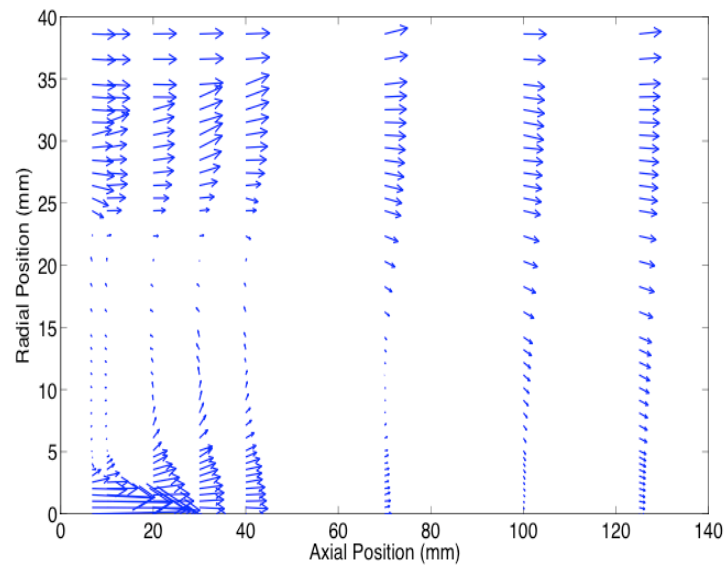


(a)

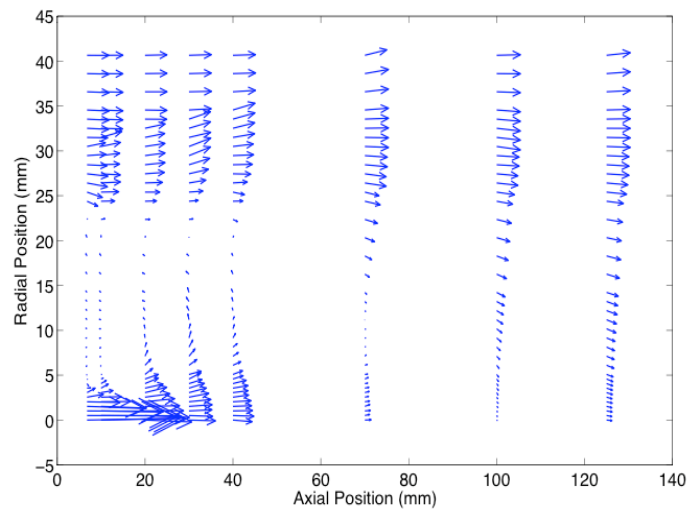


(b)

Figure 4.6: Mean tangential velocity contour plots. (a) Computational (b) Experimental.



(a)



(b)

Figure 4.7: (a) Experimental and (b) computational statistically steady state velocity vector field in the recirculation zone behind the bluff-body.

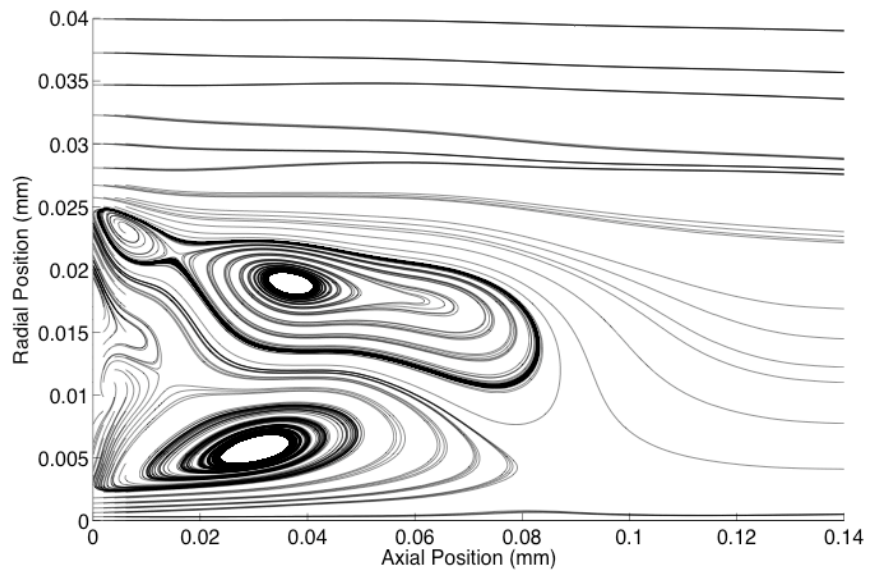


Figure 4.8: Computed statistically steady state streamlines for the non-reacting swirling bluff-body flow.

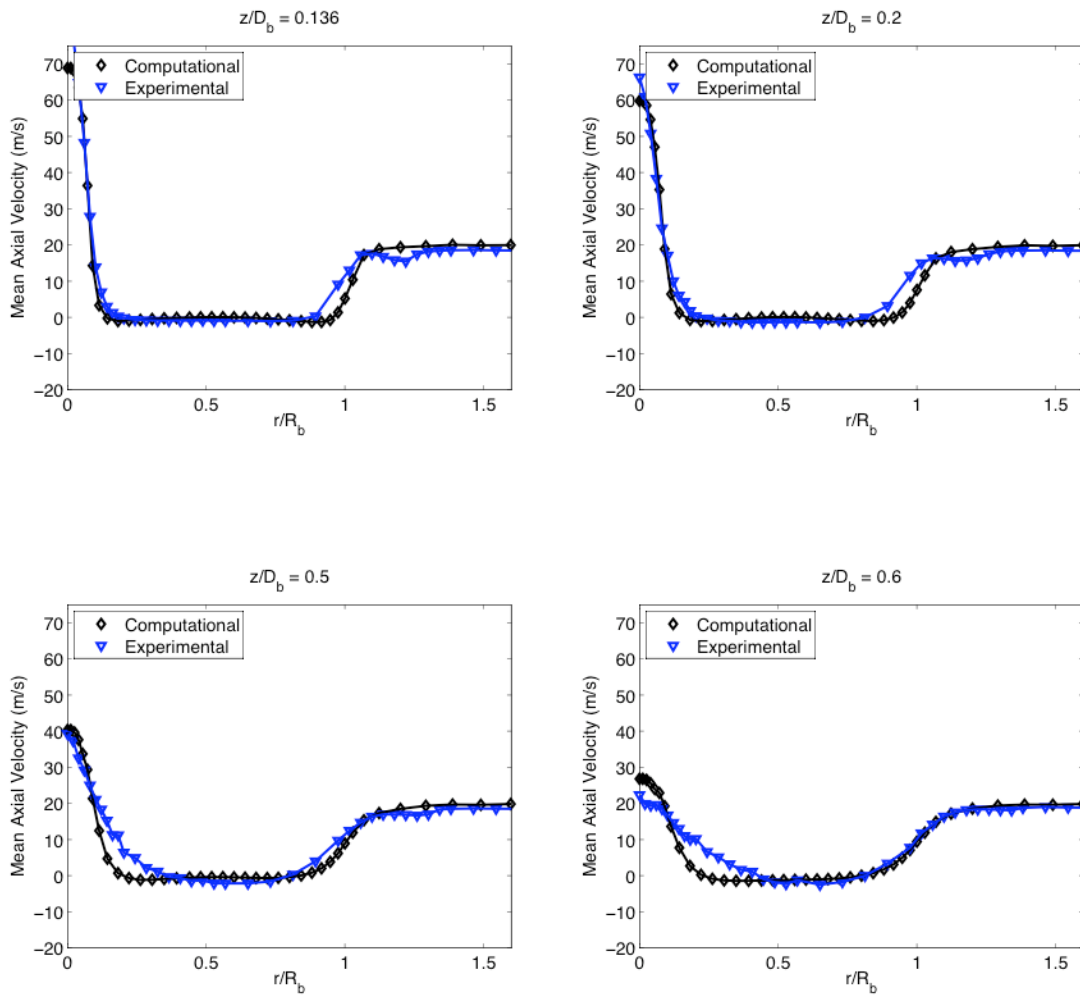


Figure 4.9a: Mean axial velocity profiles at the axial distances of $z/D_b = 0.136$, $z/D_b = 0.2$, $z/D_b = 0.5$ and $z/D_b = 0.6$ from left to right and top to bottom, respectively.

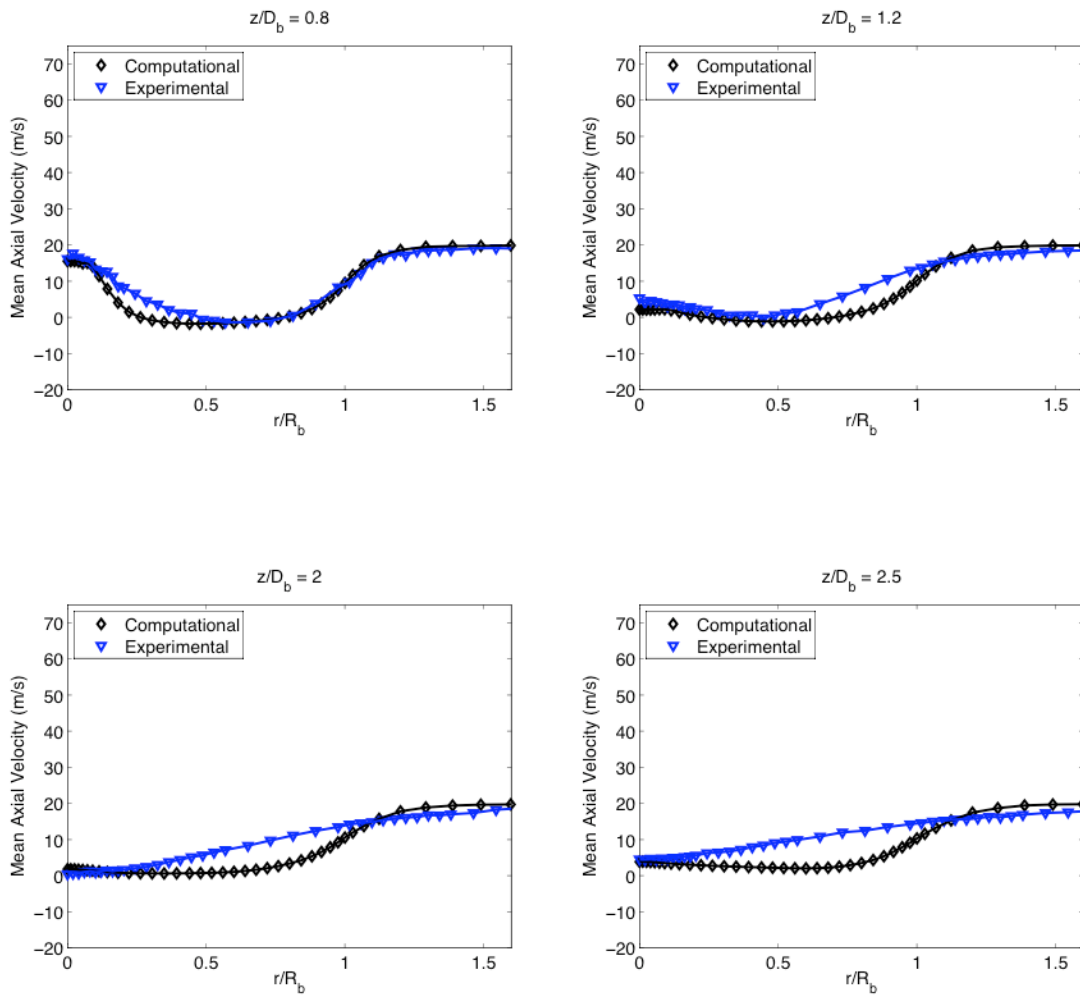


Figure 4.9b: Mean axial velocity profiles at the axial distances of $z/D_b = 0.8$, $z/D_b = 1.2$, $z/D_b = 2$ and $z/D_b = 2.5$ from left to right and top to bottom, respectively.

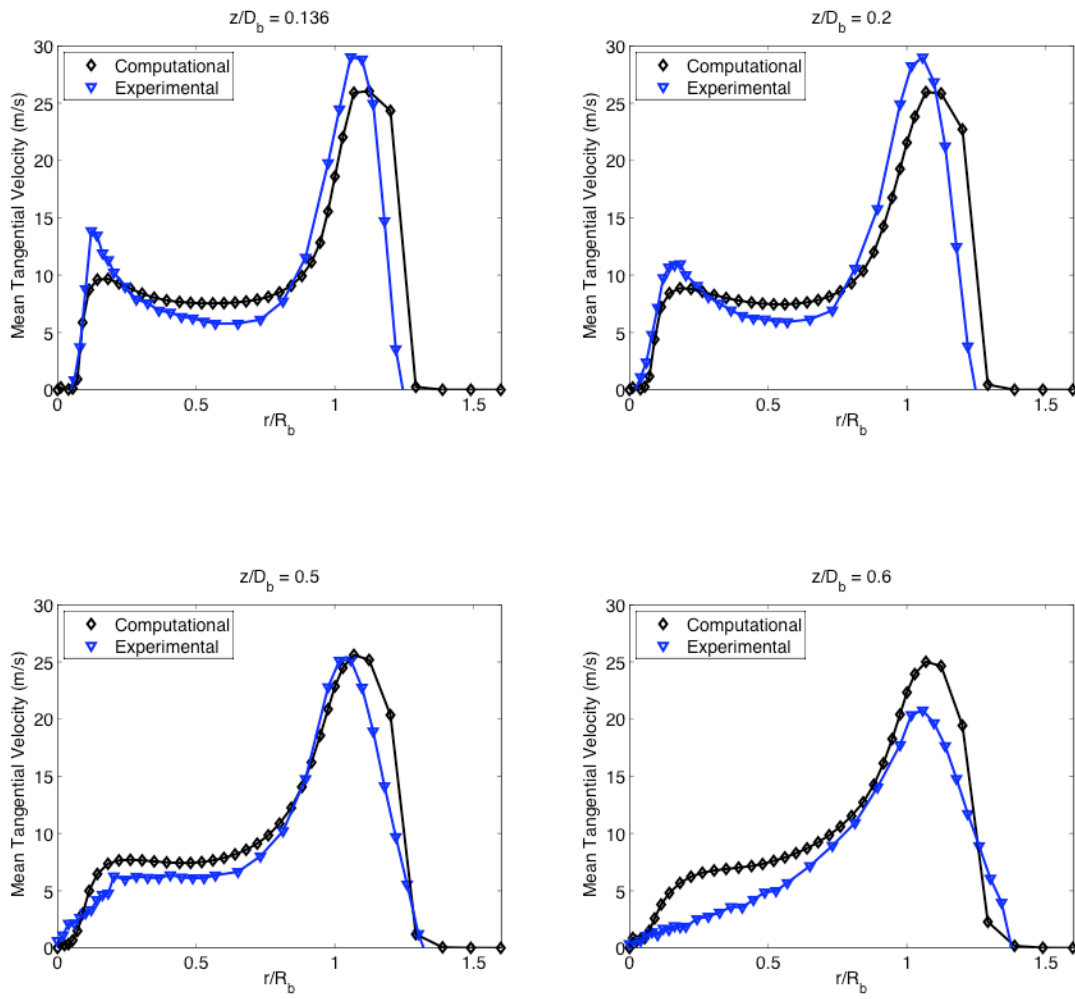


Figure 4.10a: Statistically steady mean tangential velocity profiles at the axial distances of $z/D_b = 0.136$, $z/D_b = 0.2$, $z/D_b = 0.5$ and $z/D_b = 0.6$ from left to right and top to bottom, respectively.

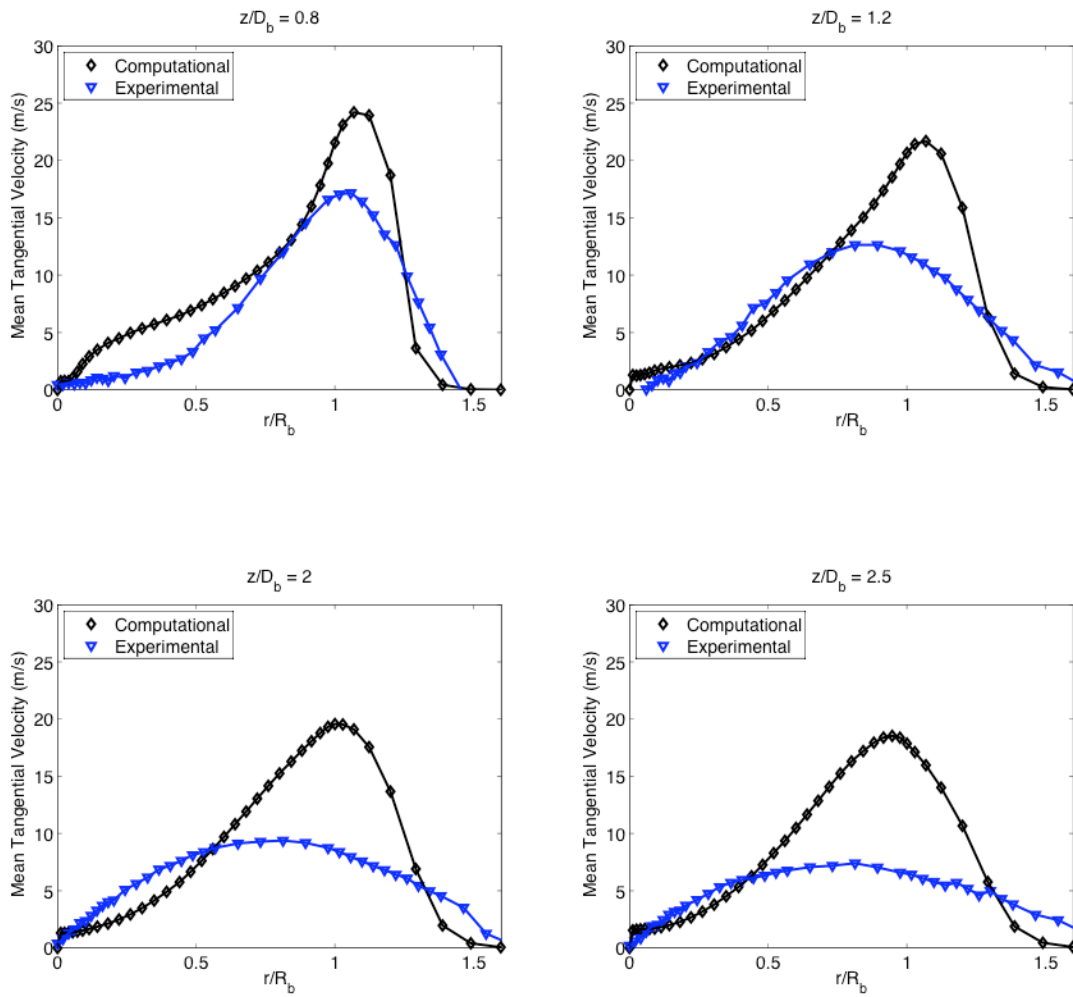


Figure 4.10b: Statistically steady mean tangential velocity profiles at the axial distances of $z/D_b = 0.8$, $z/D_b = 1.2$, $z/D_b = 2$ and $z/D_b = 2.5$ from left to right and top to bottom, respectively.

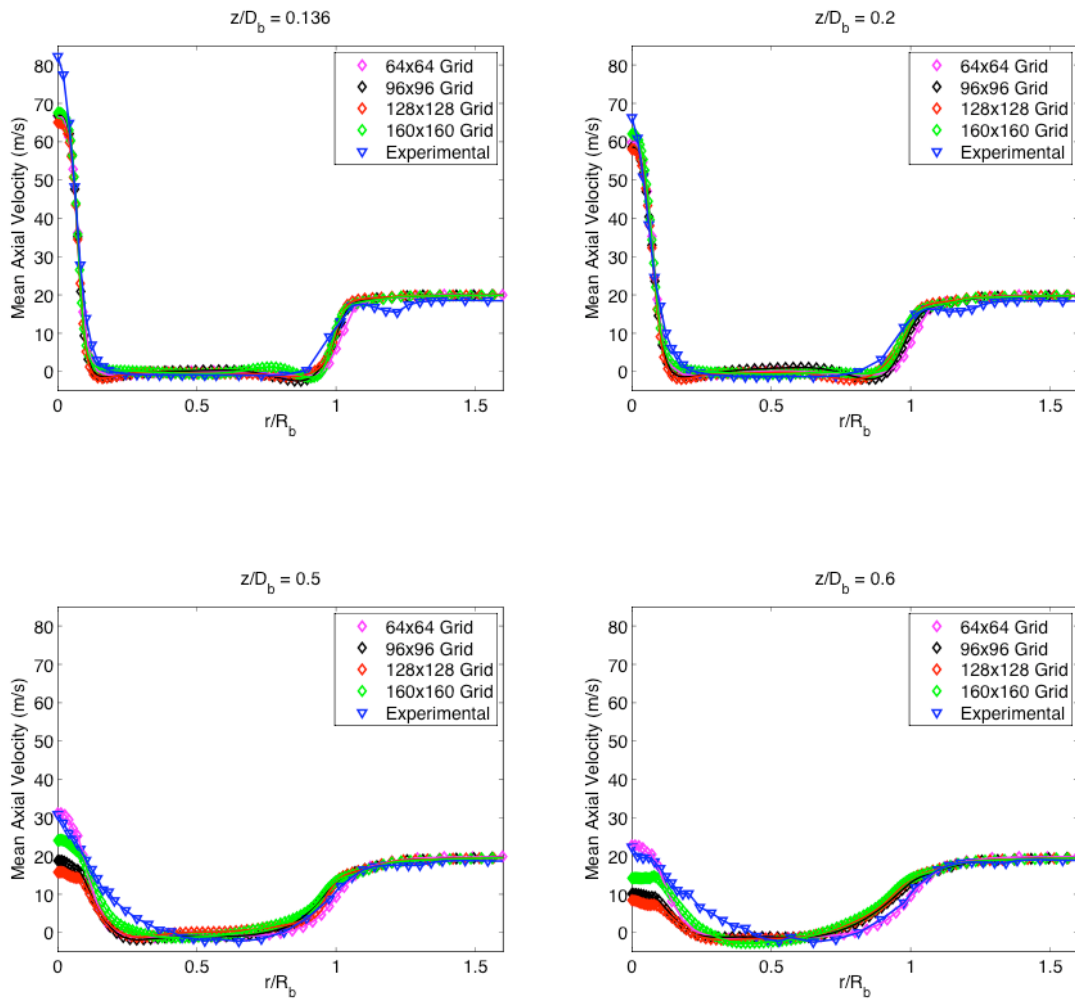


Figure 4.11a: Statistically steady mean axial velocity profiles computed using the grid resolutions of 64x64, 96x96, 128x128 and 160x160 at the axial distances of $z/D_b = 0.136$, $z/D_b = 0.2$, $z/D_b = 0.5$ and $z/D_b = 0.6$ from left to right and top to bottom, respectively.

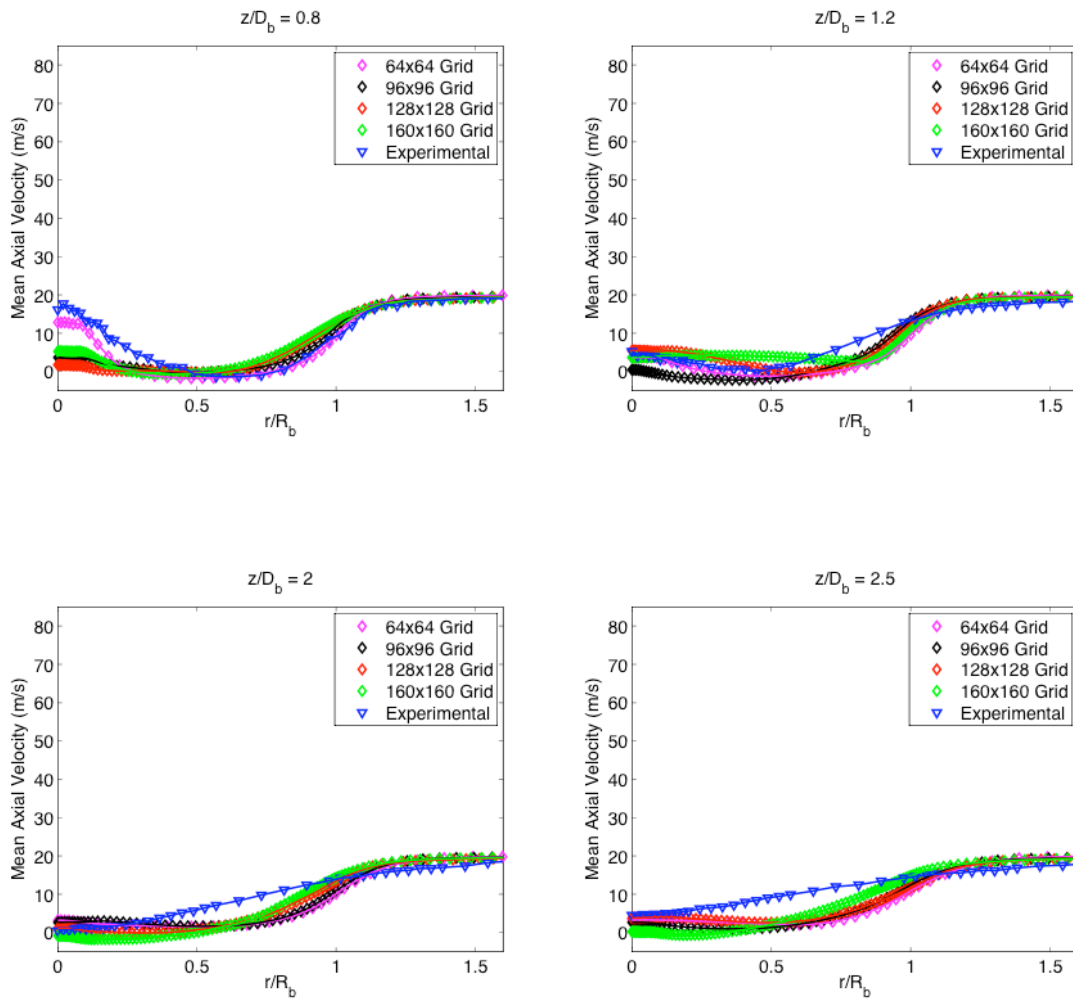


Figure 4.11b: Statistically steady mean axial velocity profiles computed using the grid resolutions of 64x64, 96x96, 128x128 and 160x160 at the axial distances of $z/D_b = 0.8$, $z/D_b = 1.2$, $z/D_b = 2.0$ and $z/D_b = 2.5$ from left to right and top to bottom, respectively.

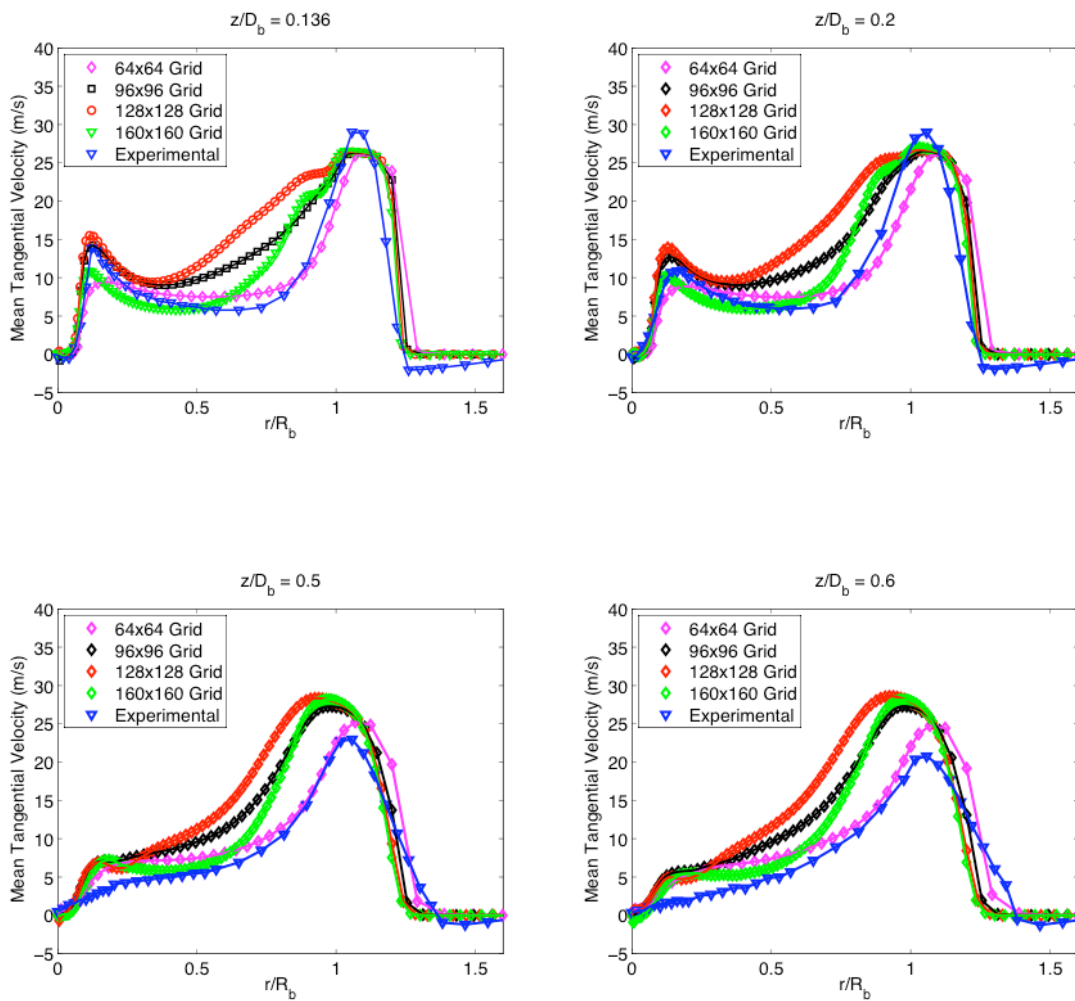


Figure 4.12a: Statistically steady mean tangential velocity profiles computed using the grid resolutions of 64x64, 96x96, 128x128 and 160x160 at the axial distances of $z/D_b = 0.136$, $z/D_b = 0.2$, $z/D_b = 0.5$ and $z/D_b = 0.6$ from left to right and top to bottom, respectively.

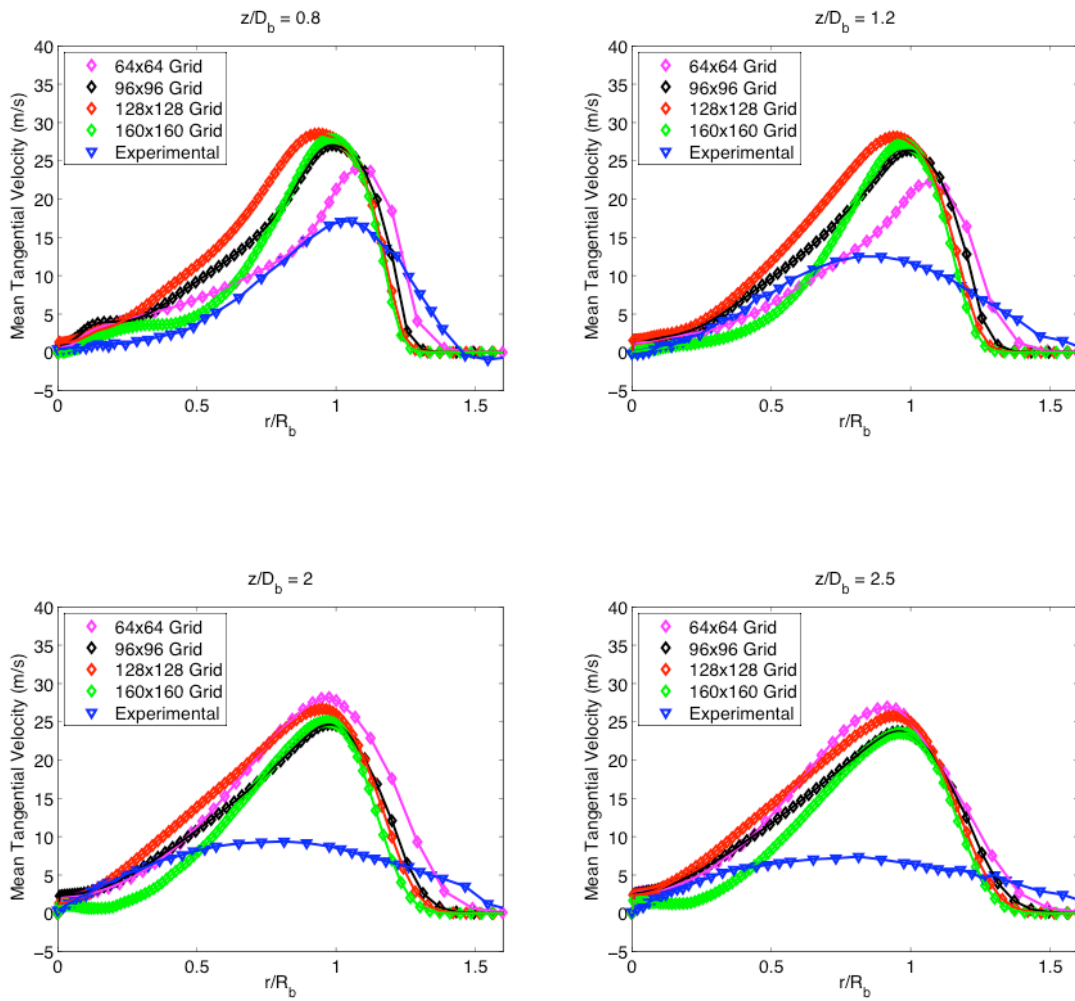


Figure 4.12b: Statistically steady mean tangential velocity profiles computed using the grid resolutions of 64x64, 96x96, 128x128 and 160x160 at the axial distances of $z/D_b = 0.8$, $z/D_b = 1.2$, $z/D_b = 2.0$ and $z/D_b = 2.5$ from left to right and top to bottom, respectively.

Chapter 5

CONCLUSIONS AND COMMENTS

PDF simulations are performed for the non-reacting swirling bluff-body flow studied experimentally by Masri et al. [1]. The velocity-turbulence frequency PDF model equations are solved a consistent finite-volume/particle-based Monte Carlo method. The finite-volume method is based on the SIMPLE algorithm coded by Peric. The new consistent hybrid algorithm has been shown to be more robust than the earlier version especially for the non-reacting and reacting bluff-body flow [10]. This is the first step in assessing the performance of the PDF approach for the challenging swirl burner simulations and aims to lay foundations for a future study in which reacting swirl burners will be simulated.

Since the hybrid method is designed to solve the statically stationary flows, it is first shown that the computed results reach a statistically steady state. For this purpose, the mean axial velocity and mean turbulent kinetic energy are monitored at selected six points in the recirculation zone. It is found that the computational results reach a statically stationary state in about 2500 particle time steps on a moderately fine grid, e.g., 64x64 grid, in terms of mean fields. After that the computational results are compared with the experimental data qualitatively for the non-reacting swirling bluff body flow labelled as N16S159 by Masri et al. [1]. For this purpose, the axial velocity contours and velocity vector fields are compared. It is found that the present results are in good qualitative agreement with the experimental data. The then grid convergence is examined. For this purpose, the computations are repeated using successively refined grids. It is found that the mean fields compare reasonably well with the experimental data on all the grids but a full grid convergence is not achieved due to vortex shedding occurring behind the bluff-body at the shear layer between the bluff-body, swirl and co-flow region. This behaviour has not been observed experimentally and it is not clear at this point whether this unphysical behaviour is due to numerical error or due to the turbulence model employed

here. It is emphasized here that similar unphysical vortex shedding behaviour has been also observed in PDF simulations of the non-reacting and non-swirling bluff-body flow studied by Jenny et al. [14]. The resolution of this problem requires further study and it is deferred to the future studies.

It is found that 30 CPU hours are needed to carry out a PDF simulation for swirling bluff-body flow simulations on a P-IV PC computer nodes of Hattusas HPC at Koc University.

BIBLIOGRAPHY

- [1] Y. M. Al-Abdeli, and A. R. Masri. Recirculation and flowfield regimes of unconfined non-reacting swirling flows. *Experimental Thermal and Fluid Science*, 27:655-665, 2003.
- [2] S. V. Alekseenko, V. M. Dulin, Y. S. Kozorezov, and D. M. Markovich. Effect of axisymmetric forcing on the structure of a swirling turbulent jet. *International Journal of Heat and Fluid Flow*, 29:1969-1715, 2008.
- [3] J. C. Broda, S. Seo, R. J. Santoro, G. Shirhattikar, and V. Yang. *Proc. Combust. Inst.*, 27:1849-1856, 1998.
- [4] L. S. Caretto, A. D. Gosman, S. V. Patankar, and D. B. Spalding. Two calculation procedures for steady, three-dimensional flows with recirculation. *3rd Int Conf on Numerical Methods in Fluid Mechanics*, 1972.
- [5] B. B. Dally, D. F. Fletcher, and A. R. Masri. Modelling of turbulent flames stabilised on a bluff-body. *Combust. Theory Modelling*, 2:193-219, 1998.
- [6] C. Dopazo. Recent developments in PDF methods, in: P.A. Libby, F.A. Williams (Eds.), *Turbulent Reacting Flows*, Academic Press, London, 1994, p. 375, 2003.
- [7] T. D. Dreeben and S. B. Pope. Nonparametric estimation of mean fields with application to particle methods for turbulent flows. *Cornell Report FDA 92-13*, 1992.
- [8] D.C. Haworth and S. B. Pope. A generalized langevin model for turbulent flows. *Phys. Fluids*, 29:387-405, 1986.
- [9] H. El-Asrag, and S. Menon. Large eddy simulations of bluff-body stabilized swirling non-premixed flames. *Proceedings of the Combustion Institute*, 31:1747-1754, 2007.

- [10] O. Eren. M.S. Thesis, Department of Computational Sciences and Engineering, Koc University, 2006.
- [11] Ford Motor Company, Annular report, 2009.
- [12] A.E. German and T. Mahmud. Modelling of non-premixed swirl burner flow using a Reynolds-stress turbulence closure. *Fuel*, 84:583-594, 2005.
- [13] P. Jenny, S. B. Pope, M. Muradoglu, and D. A. Caughey. A hybrid algorithm for the joint pdf equation of turbulent reactive flows. *J. Comp. Phys.*, 166:218-252, 2001.
- [14] P. Jenny, M. Muradoglu, K. Liu, S.B. Pope and D.A. Caughey. PDF simulations of a bluff-body stabilized flow. *J. Comp. Phys.*, 169:1-23, 2001.
- [15] A. Kempf, W. Malasekera, K.K.J. Ranga-Dinesh and O Stein. Large eddy simulations of swirling non-premixed flames with flamelet models: A comparison of numerical methods. *Flow Turb. Combust.* 81(4):523-561, 2008.
- [16] C. Kulsheimer and H. Buchner. Combustion dynamics of turbulent swirling flames. *Combust. Flame*, 131(1-2):70-84, 2002.
- [17] W. Malalasekera, K.K.J.R. Dinesh, S.S. Ibrahim and M.P. Kirkpatrick. LES of isothermal swirling jets. *Combust. Sci. Tech.*, 179(8):1481-1525, 2007.
- [18] A. R. Masri, S. B. Pope, and B. B. Dally. Probability density function computations of a strongly swirling nonpremixed flame stabilized on a new burner. *Proceedings of the Combustion Institute*, 28:123-131, 2000.
- [19] A.R. Masri, P.A.M. Kalt and R.S. Barlow. The compositional structure of swirl-stabilised nonpremixed flames. *Combust. Flame*, 137(1-2):1-37, 2004.
- [20] A. R. Masri. <http://www.aeromech.usyd.edu.au/thermofluids>. 2009
- [21] R. McDermott and S.B. Pope SB. Parabolic edge reconstruction method (PERM) for Lagrangian particle advection. *J. Comp. Phys.*, 227(11):5447-5491, 2008.
- [22] M. Muradoglu, S. B. Pope, and D. A. Caughey. The hybrid method for the pdf equations of turbulent reactive flows: consistency conditions and correction algorithms. *J. Comp. Phys.*, 172:841-878, 2001.

- [23] M. Muradoglu, and S. B. Pope. Local time-stepping algorithm for solving the probability density function turbulence model equations. *AIAA J.*, 40: 1755-1763, 2002.
- [24] M. Peric and J. H. Ferziger. *Computational Methods for Fluid Dynamics*, 1996.
- [25] S. B. Pope. PDF methods for turbulent reactive flows. *Prog. Energy Combust Sci.*, 11:119-192, 1985.
- [26] S. B. Pope. On the relationship between stochastic lagrangian models of turbulence and second-moment closure. *Phys. Fluids*, 6:973-985, 1986.
- [27] S. B. Pope. *Turbulent Flows*, 2000.
- [28] B. Rembold, and P. Jenny. A multiblock joint PDF finite-volume hybrid algorithm for the computation of turbulent flows in complex geometries. *Journal of Computational Physics*, 220:59-87, 2006.
- [29] J. Rotta. Statistische theorie nichthomogener turbulenz. *Z. Phys.*, 129:547-572, 1951.
- [30] S. Seo. Ph.D. Thesis, Department of Mechanical Engineering, The Pennsylvania State University, University Park, PA, 1999.
- [31] O. Stein, and A. Kempf. LES of the Sydney swirl flame series: A study of vortex breakdown in isothermal and reacting flows. *Proceedings of the Combustion Institute*. 31: 1755, 1763, 2007.
- [32] O. Stein, A.M. Kempf and J. Janicka. LES of the Sydney swirling jet in a bluff-body burner. *Combust. Sci. Tech.*, 179(1-2):173-189, 2007.
- [33] N. Syred. A review of oscillation mechanism and the role of the precessing vortex core (PVC) in swirl combustion system. *Prog. Energy Combust. Sci.*, 32(2):93-161, 2006.
- [34] Q. Tang, J. Xu, and S. B. Pope. Pdf calculations of local extinction and no production in piloted-jet turbulent methane/air flames. *Proceedings of the Combustion Institute*, 28:133-139, 2000.
- [35] V. Tangirala, R. H. Chen, J. F. Driscoll. *Combust. Sci. Technol.*, 51:75-95, 1987.
- [36] P. R. Van Slooten, Jayesh, and S. B. Pope. Advances in pdf modeling for inhomogeneous turbulent flows. *Phys. Fluids*, 10:246-265, 1998.

- [37] J. Xu and S. B. Pope. Pdf calculations of turbulent nonpremixed flames with local extinction. *Combustion and Flame*, 123:281-307, 2000.

Vita

Ismail Filiz was born in Istanbul, Turkey on January 26, 1982. He received the B.S. degree in Mechanical Engineering from Koc University, Istanbul, in 2006. In October 2006, he joined to the Computational Science and Engineering Department of Koc University, Turkey as a teaching and research assistant and worked on "PDF modeling of the non-reactive swirling turbulent flows."